

# Cosmological Constraints from the Clustering of the Sloan Digital Sky Survey DR7 Luminous Red Galaxies

Beth A. Reid<sup>1,2\*</sup>, Will J. Percival<sup>3</sup>, Daniel J. Eisenstein<sup>4</sup>, Licia Verde<sup>1,5</sup>, David N. Spergel<sup>2,6</sup>, Ramin A. Skibba<sup>7</sup>, Neta A. Bahcall<sup>2</sup>, Tamas Budavari<sup>8</sup>, Joshua A. Frieman<sup>9,10</sup>, Masataka Fukugita<sup>11</sup>, J. Richard Gott<sup>2</sup>, James E. Gunn<sup>2</sup>, Željko Ivezić<sup>12</sup>, Gillian R. Knapp<sup>2</sup>, Richard G. Kron<sup>13</sup>, Robert H. Lupton<sup>2</sup>, Timothy A. McKay<sup>14</sup>, Avery Meiksin<sup>15</sup>, Robert C. Nichol<sup>3</sup>, Adrian C. Pope<sup>16</sup>, David J. Schlegel<sup>17</sup>, Donald P. Schneider<sup>18</sup>, Chris Stoughton<sup>19</sup>, Michael A. Strauss<sup>2</sup>, Alexander S. Szalay<sup>8</sup>, Max Tegmark<sup>20</sup>, Michael S. Vogeley<sup>21</sup>, David H. Weinberg<sup>22</sup>, Donald G. York<sup>13,23</sup>, Idit Zehavi<sup>24</sup>

<sup>1</sup> *Institute of Space Sciences (CSIC-IEEC), UAB, Barcelona 08193, Spain and*

*Institute for Sciences of the Cosmos (ICC), University of Barcelona, Barcelona 08028, Spain*

<sup>2</sup> *Department of Astrophysical Sciences, Princeton University, Princeton, NJ 08544, USA*

<sup>3</sup> *Institute of Cosmology and Gravitation, University of Portsmouth, Portsmouth, PO1 2EG, UK*

<sup>4</sup> *Steward Observatory, University of Arizona, 933 N. Cherry Ave., Tucson, AZ 85121, USA*

<sup>5</sup> *ICREA (Institutio Catalana de Recerca i Estudis Avancats)*

<sup>6</sup> *Princeton Center for Theoretical Science, Princeton University, Jadwin Hall, Princeton NJ 08542, USA*

<sup>7</sup> *Max-Planck-Institute for Astronomy, Königstuhl 17, D-69117 Heidelberg, Germany*

<sup>8</sup> *Department of Physics and Astronomy, The Johns Hopkins University, 3701 San Martin Drive, Baltimore, MD 21218, USA*

<sup>9</sup> *Particle Astrophysics Center, Fermilab, P.O. Box 500, Batavia, IL 60510, USA*

<sup>10</sup> *Kavli Institute for Cosmological Physics, Department of Astronomy & Astrophysics, University of Chicago, Chicago, IL 60637, USA*

<sup>11</sup> *Institute for Cosmic Ray Research, University of Tokyo, Kashiwa 277-8582, Japan*

<sup>12</sup> *Department of Astronomy, University of Washington, Box 351580, Seattle, WA 98195, USA*

<sup>13</sup> *Department of Astronomy and Astrophysics, The University of Chicago, 5640 South Ellis Avenue, Chicago, IL 60615, USA*

<sup>14</sup> *Departments of Physics and Astronomy, University of Michigan, Ann Arbor, MI, 48109, USA*

<sup>15</sup> *SUPA; Institute for Astronomy, University of Edinburgh, Royal Observatory, Blackford Hill, Edinburgh, EH9 3HJ, UK*

<sup>16</sup> *Los Alamos National Laboratory, PO Box 1663, Los Alamos, NM 87545, USA*

<sup>17</sup> *Lawrence Berkeley National Lab, 1 Cyclotron Road, MS 50R5032, Berkeley, CA 94720, USA*

<sup>18</sup> *Department of Astronomy and Astrophysics, The Pennsylvania State University, University Park, PA 16802, USA*

<sup>19</sup> *Fermilab PO Box 500, Batavia, IL 60510, USA*

<sup>20</sup> *Department of Physics, Massachusetts Institute of Technology, Cambridge, Massachusetts, 02139, USA*

<sup>21</sup> *Department of Physics, Drexel University, Philadelphia, PA 19104, USA*

<sup>22</sup> *Department of Astronomy, The Ohio State University, 140 West, 18th Avenue, Columbus, OH 43210, USA*

<sup>23</sup> *The Enrico Fermi Institute, The University of Chicago, 5640 South Ellis Avenue, Chicago, IL 60615, USA*

<sup>24</sup> *Department of Astronomy, Case Western Reserve University, Cleveland, OH 44106, USA*

14 October 2009

## ABSTRACT

We present the power spectrum of the reconstructed halo density field derived from a sample of Luminous Red Galaxies (LRGs) from the Sloan Digital Sky Survey Seventh Data Release (DR7). The halo power spectrum has a direct connection to the underlying dark matter power for  $k \leq 0.2 h \text{ Mpc}^{-1}$ , well into the quasi-linear regime. This enables us to use a factor of  $\sim 8$  more modes in the cosmological analysis than an analysis with  $k_{max} = 0.1 h \text{ Mpc}^{-1}$ , as was adopted in the SDSS team analysis of the DR4 LRG sample (Tegmark et al. 2006). The observed halo power spectrum for  $0.02 < k < 0.2 h \text{ Mpc}^{-1}$  is well-fit by our model:  $\chi^2 = 39.6$  for 40 degrees of freedom for the best-fitting  $\Lambda$ CDM model. We find  $\Omega_m h^2 (n_s/0.96)^{1.2} = 0.141^{+0.010}_{-0.012}$  for a power law primordial power spectrum with spectral index  $n_s$  and  $\Omega_b h^2 = 0.02265$  fixed, consistent with CMB measurements. The halo power

\* E-mail: beth.ann.reid@gmail.com

spectrum also constrains the ratio of the comoving sound horizon at the baryon-drag epoch to an effective distance to  $z = 0.35$ :  $r_s/D_V(0.35) = 0.1097^{+0.0039}_{-0.0042}$ . Combining the halo power spectrum measurement with the WMAP 5 year results, for the flat  $\Lambda$ CDM model we find  $\Omega_m = 0.289 \pm 0.019$  and  $H_0 = 69.4 \pm 1.6 \text{ km s}^{-1} \text{ Mpc}^{-1}$ . Allowing for massive neutrinos in  $\Lambda$ CDM, we find  $\sum m_\nu < 0.62 \text{ eV}$  at the 95% confidence level. If we instead consider the effective number of relativistic species  $N_{eff}$  as a free parameter, we find  $N_{eff} = 4.8^{+1.8}_{-1.7}$ . Combining also with the Kowalski et al. (2008) supernova sample, we find  $\Omega_{tot} = 1.011 \pm 0.009$  and  $w = -0.99 \pm 0.11$  for an open cosmology with constant dark energy equation of state  $w$ . The power spectrum and a module to calculate the likelihoods is publicly available at <http://lambda.gsfc.nasa.gov/toolbox/lrgdr/>.

**Key words:** cosmology: observations, large-scale structure of Universe, galaxies: haloes, statistics

## 1 INTRODUCTION

The past decade has seen a dramatic increase in the quantity and quality of cosmological data, from the discovery of cosmological acceleration using supernovae (Riess et al. 1998; Perlmutter et al. 1999) to the precise mapping of the cosmic microwave background (CMB) with the Wilkinson Microwave Anisotropy Probe (Page et al. 2003; Nolta et al. 2009) to the detection of the imprint of baryon acoustic oscillations (BAO) in the early universe on galaxy clustering (Eisenstein et al. 2005; Cole et al. 2005). Combining the most recent of these three cosmological probes, Komatsu et al. (2009) detect no significant deviation from the minimal flat  $\Lambda$ CDM cosmological model with adiabatic, power law primordial fluctuations, and constrain that model's parameters to within a few percent.

The broad shape of the power spectrum of density fluctuations in the evolved universe provides a probe of cosmological parameters that is highly complementary to the CMB and to probes of the expansion history (e.g., supernovae, BAO). The last decade has also seen a dramatic increase in the scope of galaxy redshift surveys. The PSCz (Saunders et al. 2000) contains  $\sim 15000$  IRAS galaxies out to  $z = 0.1$ , the 2dF Galaxy Redshift Survey (2dFGRS; Colless et al. 2001, 2003) collected 221,414 galaxy redshifts with median redshift 0.11, and the Sloan Digital Sky Survey (SDSS; York et al. 2000) is now complete with 929,555 galaxy spectra (Abazajian et al. 2009) including both main galaxies ( $\langle z \rangle \sim 0.1$ ; Strauss et al. 2002) and Luminous Red Galaxies (LRGs;  $z \sim 0.35$ ; Eisenstein et al. 2001). To harness the improvement in statistical power available now from these surveys requires stringent understanding of modeling uncertainties. The three major components of this uncertainty are the non-linear gravitational evolution of the matter density field (e.g., Zel'dovich 1970; Davis et al. 1977; Davis & Peebles 1977), the relationship between the galaxy and underlying matter density fields ("galaxy bias", e.g., Kaiser 1984; Rees 1985; Cole & Kaiser 1989), and redshift space distortions (e.g., Kaiser 1987; Davis & Peebles 1983 and Hamilton 1998 for a review).

Several major advances have enabled previous analyses of 2dFGRS and SDSS to begin to address these complications. Progress in  $N$ -body simulations (e.g., Heitmann et al. 2008), analytical methods (see Carlson et al. 2009 for an overview and comparison of many recent methods), and combinations thereof (e.g., Smith et al. 2003; Eisenstein et al. 2007b) have allowed significant progress in the study of the non-linear real space matter power spectrum. Recent power spectrum analyses have accounted for the luminosity dependence of a scale independent galaxy bias (Tegmark et al. 2004a; Cole et al. 2005), which can introduce an

artificial tilt in  $P(k)$  in surveys which are not volume-limited (Percival et al. 2004). Cresswell & Percival (2009) have recently examined the scale dependence of galaxy bias as a function of luminosity and color. Tegmark et al. (2004a) applied a matrix-based method using pseudo-Karhunen-Loève eigenmodes to measure three power spectra from the SDSS galaxy distribution, allowing a quantification of the clustering anisotropy and a more accurate reconstruction of the real-space power spectrum than can be obtained from the angle-averaged redshift space power spectrum. Non-linear redshift space distortions, caused in part by the virialized motions of galaxies in their host dark matter haloes, create features known as Fingers-of-God (FOGs) along the line of sight in the redshift space galaxy density field (Davis & Peebles 1983; Gramann et al. 1994). Both Tegmark et al. (2004a) and Cole et al. (2005) apply cluster-collapsing algorithms to mitigate the effects of FOGs before computing power spectra. Previous analyses have fit galaxy power spectra to linear (Percival et al. 2001) or non-linear matter models (Spergel et al. 2003; Tegmark et al. 2004), but did not attempt to model the scale dependence of the galaxy bias. Cole et al. (2005) introduced a phenomenological model to account for both matter non-linearity and the non-trivial relation between the galaxy power spectrum  $P_{gal}(k)$  and matter power spectrum:

$$P_{gal}(k) = \frac{1 + Qk^2}{1 + Ak} P_{lin}(k), \quad (1)$$

where  $P_{lin}$  denotes the underlying linear matter power spectrum. For the 2dFGRS analysis, Cole et al. (2005) fit  $A$  using mock galaxy catalogues and derive expected central values of  $Q$ . In the fit to the observed galaxy power spectrum, they allow  $Q$  to vary up to twice the expected value, which is supported by halo model calculations of the cosmological dependence of the galaxy  $P(k)$ . This approach appears to work well for the case of 2dFGRS galaxies because it was calibrated on mock catalogues designed to match the properties of this galaxy population; however, its application to the LRG sample in Tegmark et al. (2006), where the best-fitting  $Q$  was much larger than for 2dFGRS galaxies, is questionable (see Reid et al. 2009 and Yoo et al. 2009, but also Sánchez & Cole 2008). Moreover, Percival et al. (2007) and Cresswell & Percival (2009) have demonstrated that modeling the scale-dependent galaxy bias is required to obtain a good fit for the observed galaxy power spectrum.

In this paper we focus our efforts on accurately modeling the relationship between the galaxy and matter density fields for the SDSS LRG sample. Several authors have studied this relation using the small and intermediate scale clustering in the SDSS LRG sample (Masjedi et al. 2006; Zehavi et al. 2005; Kulkarni et al. 2007;

Wake et al. 2008; Zheng et al. 2008; Reid & Spergel 2009) and galaxy-galaxy lensing (Mandelbaum et al. 2006). The LRG selection algorithm in the SDSS (Eisenstein et al. 2001) was designed to provide a homogenous galaxy sample probing a large volume with a number density,  $\bar{n}_{LRG}$ , which maximizes the effective survey volume  $V_{eff}(k)$  on the large scales of interest,  $k \sim 0.1 h \text{ Mpc}^{-1}$ .  $V_{eff}$  is given by (Feldman et al. 1994; Tegmark 1997):

$$V_{eff}(k) = \int d^3r \left[ \frac{n(\mathbf{r})P(k)}{1 + n(\mathbf{r})P(k)} \right]^2, \quad (2)$$

where  $P(k)$  denotes the measured galaxy power spectrum,  $\bar{n}(\mathbf{r})$  the average galaxy number density in the sample at position  $\mathbf{r}$ , and the integral is over the survey volume. The total error on  $P(k)$  is minimized (i.e.,  $V_{eff}$  is maximized) when  $\bar{n}P \sim 1$ , which optimally balances cosmic variance and shot noise for a fixed number of galaxies. The LRG sample has proven its statistical power through the detection of the BAO (Eisenstein et al. 2005; Percival et al. 2007). However, parameterizing the LRG power spectrum with a heuristic model for the non-linearity (Eqn. 1) and marginalizing over fitting parameters limits our ability to extract the full cosmological information available from the power spectrum shape and can introduce systematic biases (Sánchez & Cole 2008; Dunkley et al. 2009; Verde & Peiris 2008; Reid et al. 2009).

On sufficiently large scales, we expect galaxies to be linearly biased with respect to the underlying matter density field (Mo & White 1996; Scherrer & Weinberg 1998). However, an often overlooked consequence of a sample with  $\bar{n}_{LRG}P_{LRG} \sim 1$  is that errors in the treatment of the shot noise can introduce significant changes in the measured shape of  $P_{LRG}(k)$  and can be interpreted as a scale dependent galaxy bias. In the halo model picture, the LRGs occupy massive dark matter haloes, which themselves may not be Poisson tracers of the underlying matter density field, as they form at the high peaks of the initial Gaussian density distribution (e.g., Bardeen et al. 1986). Moreover, an additional shot noise-like term is generated when multiple LRGs occupy individual dark matter haloes (Peacock & Smith 2000; Cooray & Sheth 2002). Our approach is to first eliminate the one-halo contribution to the power spectrum by identifying groups of galaxies occupying the same dark matter halo, and then to calibrate the relation between the power spectrum of the reconstructed halo density field,  $P_{halo}(k, \mathbf{p})$ , and the underlying matter power spectrum,  $P_{DM}(k)$ , using the  $N$ -body simulation results presented in Reid et al. (2009). As a result, the effects of non-linear redshift space distortions caused by pairs of galaxies occupying the same halo are diminished. However, a further complication is that LRGs occupy the massive end of the halo mass function, and velocities of isolated LRGs within their host haloes could still be quite large. The details of the relation between LRGs and the underlying matter distribution can then have a significant impact on the non-linear corrections to the power spectrum.

The DR7 LRG sample has sufficient statistical power that the details of the relation between LRGs and the underlying matter density field become important and need to be reliably modeled before attempting a cosmological interpretation of the data. This paper offers three sequential key improvements to the modeling of LRG clustering compared with Eisenstein et al. (2005) and Tegmark et al. (2006):

- We reconstruct the underlying halo density field traced by the LRGs before computing the power spectrum, while Tegmark et al. (2006) apply an aggressive FOG compression algorithm. The reconstructed halo density field power spectrum deviates from the

underlying matter power spectrum by  $< 4\%$  at  $k = 0.2 h \text{ Mpc}^{-1}$ , while the Tegmark et al. (2006) power spectrum differs by  $\sim 40\%$  at  $k = 0.2 h \text{ Mpc}^{-1}$  (Reid et al. 2009).

- We produce a large set of mock LRG catalogues drawn from  $N$ -body simulations of sufficient resolution to trace a halo mass range relevant to LRGs without significant errors in the small-scale halo clustering and velocity statistics (see Appendix A of Reid et al. 2009). We present novel consistency checks between the mock and observed LRG density fields in halo-scale higher order clustering, FOG features, and the effective shot noise.

- We use these tests along with the halo model framework to determine tight bounds on the remaining modeling uncertainties, and marginalize over these in our likelihood calculation. In contrast, Eisenstein et al. (2005) assume no uncertainty in their model LRG correlation function, and Tegmark et al. (2006) marginalize over  $Q$  in Eqn. 1 with only an extremely weak prior on  $Q$ .

This paper represents a first attempt to analyse a galaxy redshift survey with a model that accounts for the non-linear galaxy bias and its uncertainty; other approaches that utilize the galaxy distribution rather than the halo density field are in development (Yoo et al. 2009).

In this paper we present and analyse a measurement of the power spectrum of the reconstructed halo density field from the SDSS DR7 LRG sample. DR7 represents a factor of  $\sim 2$  increase in effective volume over the analyses presented in Eisenstein et al. (2005) and Tegmark et al. (2006), and covers a coherent region of the sky. Section 2 describes the measurement of the reconstructed halo density field power spectrum,  $\hat{P}_{halo}(k)$ , along with the window and covariance matrices used in our likelihood analysis. Section 3 describes the details of our model for the reconstructed halo power spectrum,  $P_{halo}(k, \mathbf{p})$ . In Section 4 we summarize the tests we have performed for various systematics in our modeling of the relation between the galaxy and dark matter density field. We quantify the expected level of uncertainty through two nuisance parameters and present several consistency checks between the model and observed reconstructed halo density field. In Section 5 we discuss the cosmological constraints from  $\hat{P}_{halo}(k)$  alone as well as in combination with WMAP5 (Dunkley et al. 2009) and the Union supernova dataset (Kowalski et al. 2008). Section 6 compares our findings with the results of previous analyses of galaxy clustering, and Section 7 summarizes our conclusions.

In a companion paper (Percival et al. prep; hereafter, P09) we measure and analyse BAO in the SDSS DR7 sample, of which the LRG sample considered here is a subset. BAO are detected in seven redshift shells, leading to a 2.7% distance measure at redshift  $z = 0.275$ , and a measurement of the gradient of the distance-redshift relation, this quantified by the distance ratio between  $z = 0.35$  and  $z = 0.2$ . We show in Section 5 that the results from these measurements are in agreement with our combined results from BAO and the shape of the power spectrum calculated using just the LRGs. The results from these different analyses will be correlated because of the overlapping data used, so they should not be combined in cosmological analyses. The best data set to be used will depend on the cosmological model to be tested. While the inclusion of 2dFGRS and main SDSS galaxies in P09 provides a higher significance detection of the BAO, we show in Section 5.4 that the full power spectrum information provides tighter constraints on both massive neutrinos and the number of relativistic species.

Throughout the paper we make use of two specific cosmological models. The simulation set described in Reid et al. (2009) and

$P(k)$	Definition	Reference
$\hat{P}_{LRG}(k)$	measured angle averaged redshift-space power spectrum of the LRGs	-
$\hat{P}_{halo}(k)$	measured power spectrum of reconstructed halo density field	-
$P_{lin}(k, \mathbf{p})$	linear power spectrum computed by CAMB	Lewis et al. (2000)
$P_{DM}(k, \mathbf{p})$	theoretical real-space non-linear power spectrum of dark matter	-
$P_{nw}(k, \mathbf{p})$	theoretical linear power spectrum without BAO (“no wiggles”)	Eisenstein & Hu (1998)
$P_{damp}(k, \mathbf{p})$	theoretical linear power spectrum with damped BAO (Eqn. 10)	Eisenstein et al. (2007b)
$P_{halo}(k, \mathbf{p})$	model for the reconstructed halo power spectrum (Eqn. 16)	Reid et al. (2009)
$P_{halo,win}(k, \mathbf{p})$	$P_{halo}(k, \mathbf{p})$ convolved with survey window function (Eqn. 5) and directly compared with $\hat{P}_{halo}(k)$ in the likelihood calculation (Eqn. 6)	Percival et al. (2007)

**Table 1.** Definitions of power spectra entering our likelihood calculation;  $\mathbf{p}$  denotes the cosmological parameters.

used to calibrate the model  $P_{halo}(k, \mathbf{p})$  adopts the WMAP5 recommended  $\Lambda$ CDM values:  $(\Omega_m, \Omega_b, \Omega_\Lambda, n_s, \sigma_8, h) = (0.2792, 0.0462, 0.7208, 0.960, 0.817, 0.701)$ . We refer to this model throughout the paper as our ‘fiducial cosmological model.’ To convert redshifts to distances in the computation of the  $\hat{P}_{halo}(k)$ , we adopt a flat  $\Lambda$ CDM cosmology with  $\Omega_m = 0.25$  and  $\Omega_\Lambda = 0.75$ . Throughout we refer to the power spectrum of several different density fields and several theoretical spectra. Table 1 summarizes their definitions.

## 2 DATA

### 2.1 LRG sample

The SDSS (York et al. 2000) is the largest galaxy survey ever produced; it used a 2.5m telescope (Gunn et al. 2006) to obtain imaging data in 5 passbands  $u, g, r, i$  and  $z$  (Fukugita et al. 1996; Gunn et al. 2006). The images were reduced (Stoughton et al. 2002; Pier et al. 2003; Ivezić et al. 2004) and calibrated (Hogg et al. 2001; Smith et al. 2002; Tucker et al. 2006; Padmanabhan et al. 2008), and galaxies were selected for follow-up spectroscopy. The second phase of the SDSS, known as SDSS-II, has recently finished, and the DR7 (Abazajian et al. 2009) sample has recently been made public. The SDSS project is now continuing with SDSS-III where the extragalactic component, the Baryon Oscillation Spectroscopic Survey (BOSS; Schlegel et al. 2009), has a different galaxy targeting algorithm. DR7 therefore represents the final data set that will be released with the original targeting and galaxy selection (Eisenstein et al. 2001; Strauss et al. 2002).

In this paper we analyse a subsample containing 110 576 Luminous Red Galaxies (LRGs; Eisenstein et al. 2001), which were selected from the SDSS imaging based on  $g, r$  and  $i$  colours, to give approximately 15 galaxies per square degree. The SDSS also targeted a magnitude limited sample of galaxies for spectroscopic follow-up (Strauss et al. 2002). The LRGs extend this main galaxy sample to  $z \simeq 0.5$ , covering a greater volume. Our DR7 sample covers 7931 deg<sup>2</sup> (including a 7190 deg<sup>2</sup> contiguous region in the North Galactic Cap), with an effective volume of  $V_{eff} = 0.26 \text{ Gpc}^3 h^{-3}$ , calculated with a model power spectrum amplitude of  $10^4 h^{-3} \text{ Mpc}^3$ . This power spectrum amplitude is approximately correct for the LRGs at  $k \sim 0.15 h \text{ Mpc}^{-1}$ . For comparison, the effective volume of the sample used by Eisenstein et al. (2005) was  $V_{eff} = 0.13 \text{ Gpc}^3 h^{-3}$ , and  $V_{eff} = 0.16 \text{ Gpc}^3 h^{-3}$  in Tegmark et al. (2006); this work represents a factor of  $\sim 2$  increase in sample size over these analyses. The sample is the same as that used in P09, and its construction follows that of Percival et al. (2007), albeit with a few improvements.

We use SDSS Galactic extinction-corrected Petrosian magni-

tudes calibrated using the “übercalibration” method (Padmanabhan et al. 2008). However, we find that the power spectrum does not change significantly when one adopts the old standard calibration instead (Tucker et al. 2006). Luminosities are K-corrected using the methodology of Blanton et al. (2003); Blanton et al. (2003b). We remove LRGs that are not intrinsically luminous by applying a cut  $M_{0.1r} < -21.8$ , where  $M_{0.1r}$  is our estimate of the absolute magnitude in the  $r$ -band for a galaxy at  $z = 0.1$ .

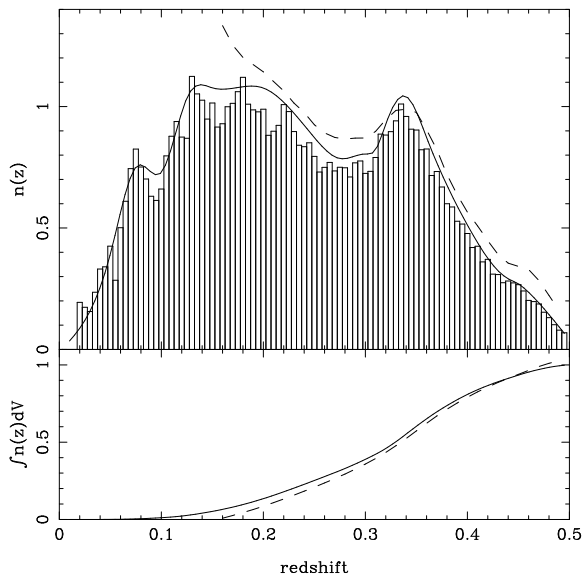
Spectroscopic LRG targets were selected using two color-magnitude cuts (Eisenstein et al. 2001). The tiling algorithm ensures nearly complete samples (Blanton et al. 2003). However, spectroscopic fiber collisions prohibit simultaneous spectroscopy for objects separated by  $< 55''$ , leaving  $\sim 7\%$  of targeted objects without redshifts (Masjedi et al. 2006). We correct for this effect as in Percival et al. (2007): for an LRG lacking a spectrum but  $55''$  from an LRG with a redshift, we assign both galaxies the measured redshift. If the LRG lacking a redshift neighbors only a galaxy from the low redshift SDSS main sample, we do not assign it a redshift. These galaxies are assumed to be randomly distributed, and simply contribute to the analysis by altering the completeness, the fraction of targeted galaxies with good redshifts, in a particular region. The impact of the fiber collision correction is addressed in Appendix B3 and Appendix B4.

Fig. 1 compares the number density as a function of redshift for the LRG selection used in this paper (Percival et al. 2007) and the one used in Tegmark et al. (2006) and presented in Zehavi et al. (2005). The main differences are that our selection includes a small number of galaxies at  $z < 0.15$ , and our cut on the intrinsic luminosity of the LRGs slightly reduces the number density of galaxies at high  $z$ . The different selections produce a similar number of galaxies per unit volume, and we expect no difference between the samples on the large scale structure statistics of interest here.

### 2.2 Recovering the halo density field

In real space, the impact of more than one LRG per halo on the large scale power spectrum can be accurately modeled as an additional shot noise term (Cooray & Sheth 2002; Reid et al. 2009). However, this picture is much more complicated in redshift-space because of the velocity dispersion of the LRGs shifts them along the line of sight by  $\sim 9 h^{-1} \text{ Mpc}$  (Reid et al. 2009), and the distribution of intrahalo velocities has long tails. This shifting causes power to be shuffled between scales and causes even the largest scale modes along the line of sight to be damped by these FOG features (Davis & Peebles 1983; Peacock & Dodds 1994; Seljak 2001). We substantially reduce the impact of these effects by using the power spectrum of the reconstructed halo density field.

We follow the Counts-In-Cylinders (CiC) technique in Reid et al. (2009) to identify LRGs occupying the same halo and thereby



**Figure 1.** Fits to the redshift distributions for the LRG selection used in this work (solid curves) and the Zehavi et al. (2005)  $-23.2 < M_g < -21.2$  sample used in Tegmark et al. (2006) (dashed curves). *Upper panel:*  $n(z)$  vs redshift in units of  $10^{-4} (h^{-1} \text{Mpc})^{-3}$ . We also show the observed number density of halos in bins of  $\Delta z = 0.005$  (see Section 2.2 for details). *Lower panel:*  $N(< z) = \int dz n(z) dV / dz$  (arbitrary overall normalization).

estimate the halo density field. Two galaxies are considered neighbors when their transverse comoving separation satisfies  $\Delta r_{\perp} \leq 0.8 h^{-1} \text{Mpc}$  and their redshifts satisfy  $\Delta z / (1 + z) \leq \Delta v_p / c = 0.006$  ( $\Delta v_p = 1800 \text{ km s}^{-1}$ ). A cylinder should be a good approximation to the density contours of satellites surrounding central galaxies in redshift space, as long as the satellite velocity is uncorrelated with its distance from the halo centre and the relative velocity dominates the separation of central and satellite objects along the line of sight. Galaxies are then grouped with their neighbors by a Friends-of-Friends (FoF) algorithm. The reconstructed halo density field is defined by the superposition of the centres of mass of the CiC groups. We refer to the power spectrum of the reconstructed halo density field as  $\hat{P}_{halo}(k)$ ; it is our best estimate of the power spectrum of the haloes traced by the LRGs. For comparison we also compute the power spectrum without applying any cluster-collapsing algorithm,  $\hat{P}_{LRG}(k)$ .

Our reconstructed halo density field contains 104 337 haloes derived from 110 576 LRGs. The observed number density of halos is shown in Fig. 1. For redshifts where the number density of LRGs is  $\sim 10^{-4} (h^{-1} \text{Mpc})^{-3}$ , the total number density drops by  $\sim 6\%$ . At the high end of the redshift distribution, there is nearly a one-to-one correspondence between LRGs and halos; that is, there are very few satellite galaxies in the sample.

### 2.3 Calculating power spectra, window functions and covariances

In this paper we focus on using the angle-averaged power spectrum to derive constraints on the underlying linear theory power spectrum. On linear scales the redshift space power spectrum is proportional to the real space power spectrum (Kaiser 1987; Hamilton 1998). Our halo density field reconstruction mitigates the effects of FOGs from objects occupying the same halo. Though we do not explore it here, we expect that our halo density field reconstruction

will be useful to an analysis of redshift-space anisotropies (e.g., Hatton & Cole 1999).

The methodology for calculating the power spectrum of the reconstructed halo density field,  $\hat{P}_{halo}(k)$ , is based on the Fourier method of Feldman et al. (1994). The halo density is calculated by throwing away all but the brightest galaxy where we have located a set of galaxies within a single halo. This field is converted to an over-density field by placing the haloes on a grid and subtracting an unclustered “random catalogue”, which matches the halo selection. To calculate this random catalogue, we fit the redshift distributions of the halo sample with a spline model (Press et al. 1992), and the angular mask was determined using a routine based on a HEALPIX (Górski et al. 2005) equal-area pixelization of the sphere as in (Percival et al. 2007). This procedure allows for the variation in radial selection seen at  $z > 0.38$ , which is caused by the spectroscopic features of the LRGs moving across the wavebands used in the target selection (see P09 for a fuller analysis). The haloes and randoms are weighted using a luminosity-dependent bias model that normalizes the fluctuations to the amplitude of  $L_*$  galaxies (Percival et al. 2004). To do this we assume that each galaxy used to locate a halo is biased with a linear deterministic bias model, and that this bias depends on  $M_{0.1r}$ , according to Tegmark et al. (2004a) and Zehavi et al. (2005), where  $M_{0.1r}$  is the Galactic extinction and K-corrected  $r$ -band absolute galaxy magnitude. This procedure is similar to that adopted by P09.

The power spectrum was calculated using a  $1024^3$  grid in a series of cubic boxes. A box of length  $4000 h^{-1} \text{Mpc}$  was used initially, but we then sequentially divide the box length in half and apply periodic boundary conditions to map galaxies that lie outside the box. For each box and power spectrum calculation, we include modes that lie between  $1/4$  and  $1/2$  the Nyquist frequency (similar to the method described by Cole et al. 2005), and correct for the smoothing effect of the cloud-in-cell assignment used to locate galaxies on the grid (e.g. Hockney & Eastwood 1981, chap. 5). The power spectrum is then spherically averaged, leaving an estimate of the “redshift-space” power. The upper panel of Fig. 2 shows the shot-noise subtracted bandpowers measured from the halo density field, calculated in bands linearly separated by  $\Delta k = 0.004 h \text{Mpc}^{-1}$ . This spacing is sufficient to retain all of the cosmological information.

The calculation of the likelihood for a cosmological model given the measured bandpowers  $\hat{P}_{halo}(k)$  requires three additional components determined by the survey geometry and the properties of the galaxy sample: the covariance matrix of measured bandpowers  $C_{ij}$ , the window function  $W(k_i, k_n)$ , and the model power spectrum as a function of the underlying cosmological parameters,  $P_{halo}(k, \mathbf{p})$ . The calculation of model power spectra is considered in Section 3.

The covariance matrix and corresponding correlation coefficients between bandpowers  $i$  and  $j$  are defined as

$$C_{ij} = \langle \hat{P}_{halo}(k_i) \hat{P}_{halo}(k_j) \rangle - \langle \hat{P}_{halo}(k_i) \rangle \langle \hat{P}_{halo}(k_j) \rangle$$

$$corr(k_i, k_j) = \frac{C_{ij}}{\sqrt{C_{ii} C_{jj}}} \quad (4)$$

The covariance matrix was calculated from  $10^4$  Log-Normal (LN) catalogues (Coles & Jones 1991; Cole et al. 2005). Catalogues were calculated on a  $(512)^3$  grid with box length  $4000 h^{-1} \text{Mpc}$  as in P09, where LN catalogues were similarly used to estimate covariance matrices. Unlike  $N$ -body simulations, these mock catalogues do not model the growth of structure, but instead return a density field with a log-normal distribution, similar to that seen in the real

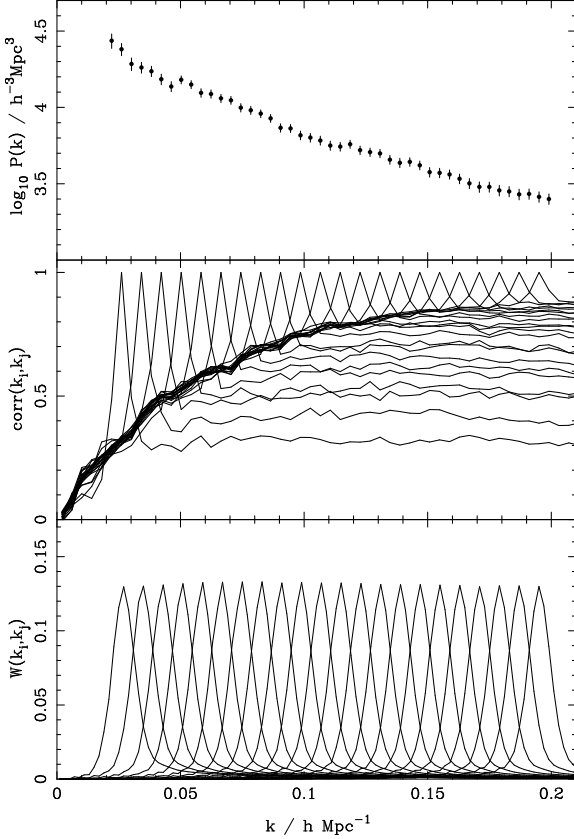


**Figure 2.** *Top panel:* Measured  $\hat{P}_{halo}(k)$  bandpowers. Error bars indicate  $\sqrt{C_{ii}}$  (Eq. 3). *Middle panel:* Correlations between data values calculated using Log-normal catalogues, assuming our fiducial cosmological model. *Bottom panel:* The normalized window function for each of our binned power spectrum values with  $0.02 < k < 0.2 h \text{ Mpc}^{-1}$ . Each curve shows the relative contribution from the underlying power spectrum as a function of  $k$  to the measured power spectrum data. The normalisation is such that the area under each curve is unity. For clarity we only plot curves for every other band power.

data. The window functions for these catalogues were matched to that of the halo catalogue. The input power spectrum was a cubic spline fit matched to the data power spectra, multiplied by a damped  $\Lambda$ CDM BAO model calculated using CAMB (Lewis et al. 2000). The recovered LN power spectra were clipped at  $5\sigma$  to remove extreme outliers which contribute less than 0.05% of the simulated power spectra, and are clearly non-Gaussian. This covariance matrix calculation matches the procedure adopted by P09. The middle panel of Fig. 2 shows the correlations expected between bandpowers calculated using this procedure. While computing the covariance matrix from realistic  $N$ -body mock LRG catalogs is still infeasible, Reid et al. (2009) showed that up to the wavenumbers considered in this paper, the covariance matrix model of Hamilton et al. (2006) containing the usual Gaussian term and a beat-coupling term to the largest scale modes provides a good fit to realistic  $N$ -body mock catalogs of several times the volume of the SDSS DR7. Both of these terms are naturally included in the LN catalogs.

As described in Cole et al. (2005), the window function can be expressed as a matrix relating the theory power spectrum for cosmological parameters  $\mathbf{p}$  and evaluated at wavenumbers  $k_n$ ,

$P_{halo}(k_n, \mathbf{p})$ , to the central wavenumbers of the observed bandpowers  $k_i$ :

$$P_{halo,win}(k_i, \mathbf{p}) = \sum_n W(k_i, k_n) P_{halo}(k_n, \mathbf{p}) - W(k_i, 0). \quad (5)$$

The term  $W(k_i, 0)$  arises because we estimate the average halo density from the sample, and is related to the integral constraint in the correlation function (Percival et al. 2007). The window function allows for the mode-coupling induced by the survey geometry. Window functions for the measured power spectrum (Eqn. 15 of Percival et al. 2004) were calculated as described in Percival et al. (2001), Cole et al. (2005), and Percival et al. (2007): an unclustered random catalogue with the same selection function as that of the haloes was Fourier transformed using the same procedure adopted for our halo overdensity field described above. The shot noise was subtracted, and the power spectrum for this catalogue was spherically averaged, and then fitted with a cubic spline, giving a model for  $W(k_i, k_n)$ . For ease of use this is translated into a matrix by splitting input and output power spectra into band powers as in Eqn. 5.

The window functions  $W(k_i, k_j)$  and the corresponding correlation coefficients for every other bandpower are shown in the lower panel of Fig. 2. In addition to the window coupling for nearby wavenumbers, there is a beat-coupling to survey-scale modes (Hamilton et al. 2006; Reid et al. 2009). That is, density fluctuations on the scale of the survey couple to the modes we can measure from the survey. However, this effect predominantly changes only the amplitude of  $\hat{P}_{halo}(k)$ , which is marginalized over through the bias parameter  $b_0^2$  in Eqn. 15 below. Fig. 2 can be compared with Fig. 10 in Percival et al. (2007), where the windows and correlations were presented for the SDSS DR5 data. For the DR5 plot, variations in the amplitude were removed leaving only the small- $k$  difference couplings. The power spectrum, window functions, and inverse covariance matrix are electronically available with the likelihood code we publicly release (see Section 5).

#### 2.4 $\hat{P}_{halo}(k)$ likelihood

We assume that the likelihood distribution of the power spectrum band powers is close to a standard multi-variate Gaussian; by the central limit theorem, this should be a good approximation in the limit of many modes per band. The final expression for the likelihood for cosmology  $\mathbf{p}$  is then

$$-2 \ln L(\mathbf{p}) = \chi^2(\mathbf{p}) = \sum_{ij} \Delta_i C_{ij}^{-1} \Delta_j, \quad (6)$$

where  $\Delta_i \equiv [(\hat{P}_{halo}(k_i) - P_{halo,win}(k_i, \mathbf{p}))]$ .

A single comoving distance-redshift relation  $\chi_{fid}(z)$ , that of a flat,  $\Omega_m = 0.25$  cosmology, is assumed to assign positions to the galaxies in our sample before computing  $\hat{P}_{halo}(k)$ . Rather than re-computing  $\hat{P}_{halo}(k)$  for each comoving distance-redshift relation to be tested, Percival et al. (2007) and P09 account for this when evaluating the likelihood of other cosmological models by altering the window function.  $D_V(z, \mathbf{p})$  (Eisenstein et al. 2005) quantifies the model dependence of the conversion between  $(\mathbf{ra}, \mathbf{dec}, z)$  and comoving spatial coordinates when galaxy pairs are distributed isotropically:

$$D_V(z) = \left[ (1+z)^2 D_A(z)^2 \frac{cz}{H(z)} \right]^{1/3}, \quad (7)$$

where  $D_A(z)$  is the physical angular diameter distance. Following Tegmark et al. (2006) we partially correct for the discrepancy between the fiducial model  $\chi_{fid}(z)$  and the  $\chi(z)$  of the model to be tested by introducing a single dilation of scale. To first order, changes in the cosmological distance–redshift model alter the scale of the measured power spectrum through  $D_V(z)$ , so we introduce a scale parameter that depends on this quantity,

$$a_{scl}(z) = \frac{D_V(z)}{D_V^{fiducial}(z)}. \quad (8)$$

Strictly, we should allow for variations in  $a_{scl}$  across the redshift range of the survey, as in P09. However, to first approximation we can simply allow for a single scale change at an effective redshift for the survey  $z_{eff}$ . When comparing  $\hat{P}_{halo}(k)$ , computed using  $\chi_{fid}(z)$ , with a model comoving distance–redshift relation  $\chi(z, \mathbf{p})$ , in practice we use <sup>1</sup>

$$\Delta_i = (\hat{P}_{halo}(k_i) - P_{halo,win}(k_i/a_{scl}, \mathbf{p})). \quad (9)$$

In Appendix A2 we verify that this approximation is valid for our sample with  $z_{eff} = 0.313$ .

In our cosmological analysis, we include modes up to  $k_{max} = 0.2 h \text{ Mpc}^{-1}$ , where the model power spectrum deviates from the input linear power spectrum by  $< 15\%$ . We also impose a conservative lower bound at  $k_{min} = 0.02$ , above which galactic extinction corrections (see the analysis in Percival et al. 2007), galaxy number density modeling, and window function errors should be negligible.

P09 present a detailed analysis demonstrating that the BAO contribution to the likelihood surface is non-Gaussian; this is in large part due to the relatively low signal-to-noise ratio of the BAO signature in our sample. Therefore, to match expected and recovered confidence intervals, P09 find that the covariance matrix of the LRG-only sample must be inflated by a factor  $1.1^2 = 1.21$ . Though our likelihood surface incorporates constraints from the shape of the power spectrum, for which the original covariance matrix should be accurate, we conservatively multiply the entire covariance matrix by this factor required for the BAO constraints throughout the analysis. Therefore our constraints likely slightly underestimate the true constraints available from the data. This factor is already included in the electronic version we release with the full likelihood code.

### 3 MODELING THE HALO POWER SPECTRUM

We consider three effects that cause the shape of  $P_{halo}(k, \mathbf{p})$  to deviate from the linear power spectrum,  $P_{lin}(k, \mathbf{p})$ , for cosmological parameters  $\mathbf{p}$ . We will assume that these modifications of the linear power spectrum can be treated independently. These effects are the damping of the BAO, the change in the broad shape of the power spectrum because of non-linear structure formation, and the bias because we observe galaxies in haloes in redshift space rather than the real space matter distribution. We also need to consider the evolution of these effects with redshift. While in principle the first two effects result from the same non-linear gravitational evolution, we find that in practice the analytic approximations we use are more accurate when these effects are treated separately since the

<sup>1</sup> This correction was incorrectly applied in previous versions of COSMOMC, and is corrected in the code we release. This correction is primarily important for constraining the BAO scale rather than the turnover scale, and so previous analyses with COSMOMC should be minimally affected.

amplitude of BAO damping depends on the tracer or whether one is considering them in real or redshift space. The nuisance parameters we introduce account for any small cosmology dependence of the smooth component of the relationship between the halo and underlying matter power spectra.

Reid et al. (2009) construct a large set of mock LRG catalogues based on  $N$ -body simulations evaluated at a single cosmological model  $\mathbf{p}_{fid}$ . We use these catalogues to calibrate the model halo power spectrum, and make detailed comparisons between the observed and mock density fields in Appendix B.

#### 3.1 BAO damping

The primary effect of non-linear structure formation and peculiar velocities on the BAOs is to damp them at large  $k$ . Eisenstein et al. (2007b) showed that this can be accurately modelled as a Gaussian smoothing, where

$$P_{damp}(k, \mathbf{p}, \sigma) = P_{lin}(k, \mathbf{p})e^{-\frac{k^2\sigma^2}{2}} + P_{nw}(k, \mathbf{p}) \left(1 - e^{-\frac{k^2\sigma^2}{2}}\right). \quad (10)$$

Here  $P_{lin}(k, \mathbf{p})$  is the linear matter power spectrum computed by CAMB (Lewis et al. 2000) and shown in the upper left panel of Fig. 3 for our fiducial cosmological model.  $P_{nw}(k, \mathbf{p})$ , defined by Eqn. 29 of Eisenstein & Hu (1998), is a smooth version of  $P_{lin}(k, \mathbf{p})$  with the baryon oscillations removed. The upper right panel of Fig. 3 shows the ratio  $P_{lin}(k)/P_{nw}(k)$  for our fiducial cosmology. The amplitude of the damping is set by  $\sigma$  and depends on the cosmological parameters, whether the power spectrum is in real or redshift space, and whether we are considering the matter or a tracer like the LRGs. We fix  $\sigma_{halo}$ , i.e., the value of  $\sigma$  appropriate for the reconstructed halo density field, using fits to the reconstructed halo density field power spectrum in the mock LRG catalogues presented in Reid et al. (2009) and shown here in Fig. 4. We have checked that the likelihood surface is unaltered when  $\sigma_{halo}$  is varied by  $\pm 10\%$ , (i.e., the error on the mock catalog fit to  $\sigma_{halo}$ ), and also in the  $\Lambda$ CDM case when  $\sigma$  is allowed to vary with cosmology  $\mathbf{p}$  according to the dependence given in Eisenstein et al. (2007b). In Appendix A3 we also show that using a spline fit to  $P_{lin}$  instead of the Eisenstein & Hu (1998) formula for  $P_{nw}$  does not affect the likelihood surface in the region of interest.

#### 3.2 Non-linear structure growth

As the small perturbations in the early universe evolve, gravitational instability drives the density field non-linear, and power on small scales is enhanced as structures form. HALOFIT (Smith et al. 2003) provides an analytic formalism to estimate the real space non-linear matter power as a function of the underlying linear matter power spectrum. While Eqn. 10 accounts for the effects of non-linear growth of structure on the BAO features in  $P_{halo}(k, \mathbf{p})$ , HALOFIT provides a more accurate fit to the smooth component of the non-linear growth in the quasi-linear regime ( $k \leq 0.2$ ) when evaluated with an input spectrum  $P_{nw}(k, \mathbf{p})$  rather than the linear matter power spectrum containing BAO wiggles:

$$r_{halofit}(k, \mathbf{p}) \equiv \frac{P_{halofit,nw}(k, \mathbf{p})}{P_{nw}(k, \mathbf{p})} \quad (11)$$

$$P_{DM,halofit}(k, \mathbf{p}) = P_{damp}(k, \mathbf{p}, \sigma_{DM}(\mathbf{p}))r_{halofit}(k, \mathbf{p}) \quad (12)$$

Eqn. 12 is our modified HALOFIT model real space power spectrum, using Eqn. 10 to account for BAO damping and HALOFIT for the smooth component. The bottom left panel of Fig. 3 shows that  $P_{DM}(k)/P_{damp}(k, \sigma_{DM})$  and  $r_{halofit}$  agree at the  $\sim 1.5\%$

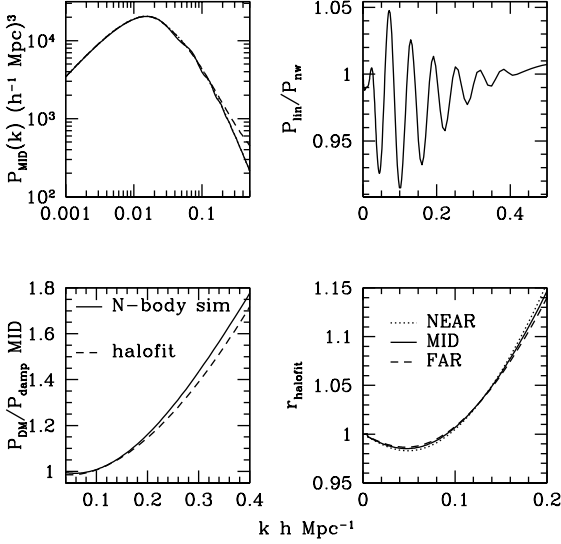


**Figure 3.** *Upper left panel:* Power spectra for the fiducial cosmology. The solid curve is  $P_{\text{lin}}(k)$  and the dashed curve is  $P_{\text{nw}}(k)r_{\text{halofit}}$ , the non-linear power spectrum from HALOFIT using  $P_{\text{nw}}(k)$  as the input. *Upper right panel:*  $P_{\text{lin}}(k)/P_{\text{nw}}(k)$ . *Bottom left panel:*  $P_{\text{DM}}(k)/P_{\text{damp}}(k, \sigma_{\text{DM}})$  measured in  $N$ -body simulation snapshots at  $z_{\text{MID}}$ , reported in Reid et al. (2009), compared with the smooth correction predicted by HALOFIT,  $r_{\text{halofit}}$ . *Bottom right panel:*  $r_{\text{halofit}}$  at  $\{z_{\text{NEAR}}, z_{\text{MID}}, z_{\text{FAR}}\} = \{0.235, 0.342, 0.421\}$ .

level for  $k \leq 0.2$  in our fiducial cosmology. Since we normalize the final model using our  $N$ -body mock catalogues at the fiducial cosmology  $\mathbf{p}_{\text{fid}}$ , in practice HALOFIT only provides the cosmological dependence of the non-linear correction to the matter power spectrum:

$$r_{\text{DM,damp}}(k, \mathbf{p}) = \frac{r_{\text{halofit}}(k, \mathbf{p})}{r_{\text{halofit}}(k, \mathbf{p}_{\text{fid}})} \frac{P_{\text{DM}}(k, \mathbf{p}_{\text{fid}})}{P_{\text{damp}}(k, \mathbf{p}_{\text{fid}}, \sigma_{\text{DM}})}. \quad (13)$$

$r_{\text{DM,damp}}(k, \mathbf{p})$  is our model for the ratio of the non-linear matter power spectrum to the damped linear power spectrum. The normalization of  $r_{\text{DM,damp}}$  (second term on the right hand side of Eq. 13) accounts for the small offset between the  $N$ -body and HALOFIT results in Fig. 3 at the fiducial cosmology. In the space of cosmologies consistent with the data, the small cosmology-dependence of this correction is primarily through  $\sigma_8$ . In Section 5.2 we find that the LRG-only likelihood surface is independent of the assumed value of  $\sigma_8$  over the range 0.7 to 0.9.

### 3.3 Halo bias

In our likelihood calculation we marginalize over the overall amplitude of  $\hat{P}_{\text{halo}}(k)$ , so in this Section we are concerned only with the scale dependence of the relation between the reconstructed halo and matter power spectra. Smith et al. (2007) show that the scale dependence of halo bias in real space is large for the most massive haloes, but should be rather weak for the halo mass range which host the majority of the LRGs; Matsubara (2008) demonstrates this analytically in redshift space in the quasi-linear regime. Indeed, Reid et al. (2009) find that the power spectrum of the (redshift space) reconstructed halo density field is nearly linearly biased with respect to the underlying real space matter power spectrum for  $k < 0.2 h \text{Mpc}^{-1}$  and our fiducial  $\Lambda\text{CDM}$  model, and we assume

this should remain approximately true in the narrow range of cosmologies consistent with the data. For the fiducial cosmology, we can use our simulations to calibrate the relation between the halo and matter spectra:

$$r_{\text{halo,DM}}(k, \mathbf{p}_{\text{fid}}) = \frac{P_{\text{halo}}(k, \mathbf{p}_{\text{fid}})/P_{\text{damp}}(k, \mathbf{p}_{\text{fid}}, \sigma_{\text{halo}})}{P_{\text{DM}}(k, \mathbf{p}_{\text{fid}})/P_{\text{damp}}(k, \mathbf{p}_{\text{fid}}, \sigma_{\text{DM}})}. \quad (14)$$

This is our model for the smooth component of the bias between the halo and dark matter power spectra. To account for any dependence of  $r_{\text{halo,DM}}(k, \mathbf{p})$  on the cosmological model and other remaining modeling uncertainties, we introduce a smooth multiplicative correction to the final model  $P_{\text{halo}}(k, \mathbf{p})$  containing three nuisance parameters  $b_0$ ,  $a_1$  and  $a_2$ :

$$F_{\text{nuis}}(k) = b_0^2 \left( 1 + a_1 \left( \frac{k}{k_*} \right) + a_2 \left( \frac{k}{k_*} \right)^2 \right) \quad (15)$$

where we set  $k_* = 0.2 h \text{Mpc}^{-1}$ . The parameter  $b_0$  is the effective bias of the LRGs at the effective sample redshift,  $z_{\text{eff}}$ , relative to  $L^*$  galaxies (Eqn. 18 of Percival et al. 2004). In Section 4 we will use consistency checks between the observed and mock catalogue galaxy density fields as well as the halo model framework to establish the allowed region of  $a_1 - a_2$  parameter space. An allowed trapezoidal region in  $a_1 - a_2$  space is completely specified through two parameters,  $u_{0,1}$  and  $u_{0,2}$ . These two parameters specify the maximum absolute deviation allowed by  $F_{\text{nuis}}(k)/b_0^2$  away from 1 for  $k \leq 0.1$  ( $u_{0,1}$ ) and  $0.1 \leq k \leq 0.2$  ( $u_{0,2}$ ). We have verified that for the two largest systematic uncertainties discussed in Section 4, the effective shot noise subtraction and power damping by central LRG intrahalo velocities, the form of  $F_{\text{nuis}}(k)$  in Eq. 15 adequately describes the deviations from the fiducial model. When evaluating the likelihood of a particular cosmological model we marginalize analytically over  $b_0$  using a flat prior on  $b_0^2 \geq 0$ , and we marginalize numerically over the allowed  $a_1 - a_2$  region with a flat prior in this region. We discuss the impact of these priors on the cosmological constraints in Appendix C.

### 3.4 Model fits and evolution with redshift

Our final model halo power spectrum at fixed redshift treats each of the three non-linear effects independently: Eqn. 10 converts the linear power spectrum to the damped linear power spectrum,  $r_{\text{DM,damp}}$  converts the damped linear power spectrum to the real space non-linear matter power spectrum,  $r_{\text{halo,DM}}$  converts the real space non-linear matter power spectrum to the redshift space reconstructed halo density field power spectrum (assuming this relation is cosmology independent), and  $F_{\text{nuis}}(k)$  allows for smooth deviations from our model due to modeling errors, uncertainties, and unaccounted cosmological parameter dependencies:

$$P_{\text{halo}}(k, \mathbf{p}) = P_{\text{damp}}(k, \mathbf{p}) r_{\text{DM,damp}}(k, \mathbf{p}) \times r_{\text{halo,DM}}(k, \mathbf{p}_{\text{fid}}) F_{\text{nuis}}(k). \quad (16)$$

For this multiplicative model, the  $P_{\text{DM}}(k, \mathbf{p}_{\text{fid}})/P_{\text{damp}}(k, \mathbf{p}_{\text{fid}}, \sigma_{\text{DM}})$  terms from Eqns. 13 and 14 cancel, so calibration of the model only requires fits to  $\sigma_{\text{halo}}$  and  $P_{\text{halo}}(k, \mathbf{p}_{\text{fid}})/P_{\text{damp}}(k, \mathbf{p}_{\text{fid}}, \sigma_{\text{halo}})$  using the mock catalogues.

The model in Eqn. 16 is strictly only valid at a single redshift. In order to match our model to the observed redshift distribution of the LRGs and their associated haloes, we use the mock halo catalogues constructed in Reid et al. (2009) at three redshift snapshots. These are centered on the NEAR ( $z_{\text{NEAR}} =$

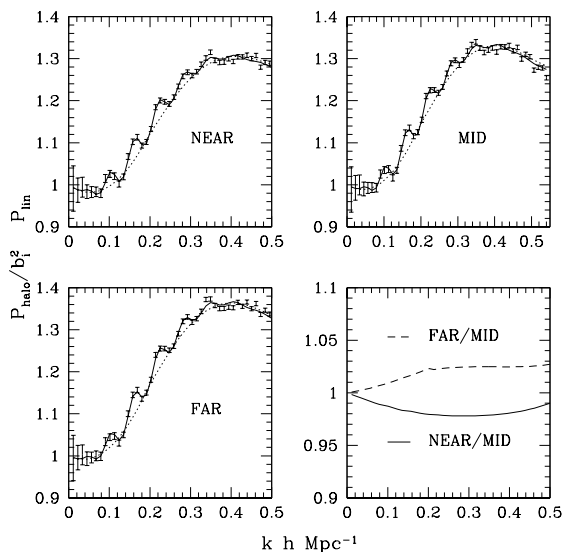


**Figure 4.** BAO-damping times polynomial fits to  $P_{halo}(k, \mathbf{p}_{fid})/b_i^2 P_{lin}(k, \mathbf{p}_{fid})$  for our mock NEAR, MID, and FAR LRG reconstructed halo density field subsamples in Reid et al. (2009);  $\{z_{NEAR}, z_{MID}, z_{FAR}\} = \{0.235, 0.342, 0.421\}$  and the  $b_i^2$  values are chosen so that this ratio is unity as  $k \rightarrow 0$ . The smooth component of these fits (dashed curves) enter our model  $P_{halo}(k, \mathbf{p})$  through Eqns. 13 and 14, while the amplitude of the BAO suppression  $\sigma_{halo}^2$  enters in Eqn. 10. *Lower right panel:* Ratio of the shape of the smooth components for the NEAR and FAR redshift subsamples to the MID redshift subsample.

0.235), MID ( $z_{MID} = 0.342$ ), and FAR ( $z_{FAR} = 0.421$ ) LRG subsamples of Tegmark et al. (2006). Fig. 4 shows our fits to  $P_{halo}(k, \mathbf{p}_{fid})/P_{lin}(k, \mathbf{p}_{fid})$  for each redshift snapshot. The model in Eq. 16 can be rewritten as

$$\frac{P_{halo}(k, \mathbf{p}_{fid})}{P_{lin}(k, \mathbf{p}_{fid})} = \frac{P_{halo}(k, \mathbf{p}_{fid})}{P_{damp}(k, \mathbf{p}_{fid})} \frac{P_{damp}(k, \mathbf{p}_{fid})}{P_{lin}(k, \mathbf{p}_{fid})}. \quad (17)$$

The first term on the right hand side is the ‘smooth’ component and equal to  $r_{DM,damp}(k, \mathbf{p}_{fid})r_{halo,DM}(k, \mathbf{p}_{fid})$ , while the second term describes the BAO damping and only depends on  $\sigma_{halo}$  in Eqn. 10. We first fit for  $\sigma_{halo}$  by including modes between  $k = 0 h \text{ Mpc}^{-1}$  and  $k = 0.2 h \text{ Mpc}^{-1}$  in the fit and marginalizing over an arbitrary fourth order polynomial to account for any smooth deviations from  $P_{damp}$  with  $k$ . We find  $\sigma_{halo, NEAR} = 9.3 h^{-1} \text{ Mpc}$ ,  $\sigma_{halo, MID} = 9.2 h^{-1} \text{ Mpc}$ , and  $\sigma_{halo, FAR} = 9.2 h^{-1} \text{ Mpc}$ . These numbers are roughly consistent with the results presented in Eisenstein et al. (2007b), and are somewhat degenerate with the smooth polynomial correction in this approach.

After fixing these values for  $\sigma_{halo}$ , we calibrate the smooth component of the model. For  $k \leq 0.2$  we fit  $P_{halo}(k, \mathbf{p}_{fid})/P_{damp}(k, \mathbf{p}_{fid}, \sigma_{halo})$  to a second order polynomial, and a fourth order polynomial for  $k \leq 0.5$ . This component of the fit is shown in the first three panels of Fig. 4 by the dotted curves, while the solid lines show the full fit to  $P_{halo}(k, \mathbf{p}_{fid})/P_{lin}(k, \mathbf{p}_{fid})$ . Both the BAO-damping and smooth increase in power with  $k$  are well described by our fits out to  $k = 0.5 h \text{ Mpc}^{-1}$ . We refer the interested reader to Reid et al. (2009) for further details.

Our final model for the reconstructed halo power spectrum is a weighted sum over our model  $P_{halo}(k, \mathbf{p})$  (Eqn. 16) from each of the NEAR, MID, and FAR redshift slices fit in Fig. 4:

$$P_{halo}(k, \mathbf{p}) = \sum_{i=NEAR, MID, FAR} w_i P_{halo}(k, \mathbf{p}, z_i), \quad (18)$$

where  $w_i$  specifies the weight of each redshift subsample. The lower right panel of Fig. 3 shows that the smooth correction for the non-linear matter power spectrum varies by  $< 1\%$  over the redshift range of the LRGs. Moreover, the lower right panel of Fig. 4 shows that the relative shape of the power spectrum of the reconstructed halo density field varies by  $\pm \sim 2.5\%$  between the redshift subsamples, so moderate biases in the determination of these weights will induce negligible changes in the predicted shape  $P_{halo}(k, \mathbf{p})$ .

In the limit that most pairs of galaxies contributing power to mode  $\mathbf{k}$  come from the same redshift, the fractional contribution to the power spectrum from a large redshift subsample is

$$w(z_{min}, z_{max}) \propto \int_{z_{min}}^{z_{max}} n^2(z) \frac{w^2(z)}{b^2(z)} \frac{dV}{dz} dz, \quad (19)$$

where  $n(z)$ ,  $b(z)$ , and  $w(z)$  specify the average number density, bias, and weight of the sample at redshift  $z$  as defined in Percival et al. (2004). Since the integrand is slowly varying with redshift, this approximation should be fairly accurate. We derive weights  $w_{NEAR} = 0.395$ ,  $w_{MID} = 0.355$ , and  $w_{FAR} = 0.250$ .

### 3.5 Comparison with fiducial model $P_{halo}(k, \mathbf{p}_{fid})$

Our fiducial  $P_{halo}(k, \mathbf{p})$  model is calibrated on simulations with the WMAP5 recommended parameters (Komatsu et al. 2009):  $(\Omega_m, \Omega_b, \Omega_\Lambda, n_s, \sigma_8, h) = (0.2792, 0.0462, 0.7208, 0.960, 0.817, 0.701)$ . For the 45 observed bandpowers satisfying  $0.02 < k < 0.2 h \text{ Mpc}^{-1}$ ,  $\chi^2 = 44.0$  if we hold nuisance parameters  $a_1 = a_2 = 0$  and choose  $b_0$  to minimize  $\chi^2$ ; our fiducial model is therefore sufficiently close to the measured  $\hat{P}_{halo}(k)$  to be used to calibrate the cosmology-dependent model. The best-fitting nuisance parameters within the allowed range that we determine in Section 4.3,  $a_1 = 0.172$  and  $a_2 = -0.198$ , lower the  $\chi^2$  to 40.9 for 42 DOF. The best-fitting model to the LRG-only likelihood presented in Section 5.1 is lower by only  $\Delta\chi^2 \approx 1.7$  for the same treatment of the three nuisance parameters.

## 4 QUANTIFYING MODEL UNCERTAINTIES AND CHECKS FOR SYSTEMATICS

While the non-linear evolution of a collisionless dark matter density field can be accurately studied using  $N$ -body simulations, there remain many uncertainties in the mapping between the galaxy and matter density field. We first review the generic halo model predictions for a galaxy power spectrum, which provide the context for exploring the uncertainties in the relation between the galaxy and matter density fields. We summarize the results of Appendix B, which presents our modeling assumptions and consistency checks between the mock catalogue and SDSS DR7 LRG density fields that constrain the level of deviation from our modeling assumptions. The ultimate goal of this Section is to establish physically-motivated constraints on the nuisance parameters  $a_1$  and  $a_2$  in Eqn. 15 by determining  $u_{0.1}$  and  $u_{0.2}$  defined in Section 3.3. These nuisance parameter constraints will then be used to compute cosmological parameter constraints in Section 5.

#### 4.1 Galaxy power spectra in the halo model

In the simplest picture for a galaxy power spectrum in the halo model, one considers a separation of the pairs into galaxies occupying the same dark matter halo, which contribute to  $P^{1h}(k)$ , and those occupying different dark matter haloes, which contribute to  $P^{2h}(k)$  (Cooray & Sheth 2002):

$$P_{gal}(k) = P_{gal}^{1h}(k) + P_{gal}^{2h}(k) \quad (20)$$

$$P_{gal}^{1h} = \int dM n(M) \frac{\langle N_{gal}(N_{gal} - 1) | M \rangle}{\bar{n}_{gal}^2} \quad (21)$$

$$P_{gal}^{2h}(k) = b_{gal}^2 P_{DM}(k). \quad (22)$$

On large scales, treating the haloes as linear tracers of the underlying matter density field (Eqn. 22) and ignoring the spatial extent of haloes in Eqn. 21 are good approximations (Reid et al. 2009). Therefore, in real space, the dominant effect of the inclusion of satellite galaxies is an excess shot noise given by Eqn. 21, though they also upweight highly biased halo pairs and slightly increase  $b_{gal}$  as well. However, in redshift space, satellite galaxies are significantly displaced along the line of sight from their host haloes by the FOGs, and power is shuffled between scales, and even the largest scale modes along the line of sight are damped by the FOG smearing. There will be residual non-linear redshift space distortions in the reconstructed halo density field from imperfect reconstruction, and potentially from peculiar motion of isolated LRGs in their host haloes as well.

#### 4.2 Summary of tests for systematics and remaining uncertainties

In the context of the halo model, both uncertainty in the distribution of galaxies in groups as it enters Eqn. 21 and uncertainty in the structure of the FOG features will introduce uncertainty in the relation between the reconstructed halo and matter density fields, and thus their power spectra. Appendices B1 and B2 discuss the modeling assumptions we have used to derive the Reid et al. (2009) mock LRG catalogues from  $N$ -body simulation halo catalogues, and state the expected impact on the relation between the reconstructed halo and matter power spectra.

Appendix B3 introduces several distinct consistency checks of the uncertainties in Appendices B1 and B2. In Section 2.2 we define the CiC group finder by which we identify haloes. We demonstrate that this group finder produces group multiplicity functions that are in good agreement between the mock and observed LRG density fields, once fiber collisions are accounted for. While this agreement demonstrates that our mock catalogues reproduce small scale higher-order clustering statistics and FOG features of the observed density field, this is not a consistency check since the mocks were designed to match these statistics. We find consistency when we compute a second CiC group multiplicity function allowing a wider separation between pairs perpendicular to the line of sight ( $\Delta r_{\perp} = 1.2 h^{-1} \text{ Mpc}$ ). If the observed satellite galaxies were significantly less concentrated than in our mock catalogues, we would detect these galaxies when  $\Delta r_{\perp}$  increases from  $0.8 h^{-1} \text{ Mpc}$  to  $1.2 h^{-1} \text{ Mpc}$ . From this comparison we conclude that residual shot noise errors from inaccurate halo density field reconstruction are  $\sim 2\%$  of the total shot noise correction and do not dominate our systematic uncertainty. The second consistency check between the mock and observed LRG catalogues is the distribution of line of sight separations between pairs of galaxies in the same CiC group (Fig B2). This check probes the accuracy of our model of the FOG

features coming from galaxies occupying the same halo, and the agreement we find indicates that the residual FOG features in the reconstructed observed and mock halo density fields will be in satisfactory agreement. Appendix B4 presents the difference between the power spectra with and without the halo density field reconstruction preprocessing step ( $\hat{P}_{halo}(k)$  and  $\hat{P}_{LRG}(k)$ , respectively). This difference agrees with the mock catalogues, provided one carefully accounts for the impact of fiber collisions. In other words, while the treatment of fiber collisions can substantially impact  $\hat{P}_{LRG}(k)$ ,  $\hat{P}_{halo}(k)$  is unaffected. In Appendix B5 we demonstrate that the luminosity weighting used to compute  $\hat{P}_{halo}(k)$  but not accounted for in the mock catalogues does not alter the effective shot noise level of  $\hat{P}_{halo}(k)$ . Appendix B6 presents evidence that the cosmology dependence of the model  $P_{halo}(k, \mathbf{p})$  is sufficiently accurate. Finally, we note that Lunnan et al. (prep) have compared the Reid et al. (2009) mock catalogue genus curve with the observed genus curves (Gott et al. 2009), and find good agreement with no free parameters.

As discussed in detail in Appendix B2, the vast majority of LRGs ( $\sim 94\%$ ) are expected to reside at the centre of their host dark matter haloes (Zheng et al. 2008; Reid et al. 2009). The principal modeling uncertainty we identify in Appendix B is the velocity of these central LRGs within their host haloes; substantial intra-halo velocities for these galaxies will suppress power in a scale-dependent manner (Fig. B1). Note that none of the tests from Appendix B can directly constrain the level of central LRG velocity dispersion.

#### 4.3 Constraints on $F_{nuis}(k)$

In Section 3.3 we introduced a quadratic function  $F_{nuis}(k)$  to account both for errors in our modeling at the fiducial cosmology and for any errors in the cosmology dependence of our model. We parametrized the amplitude of the total modeling uncertainty through  $u_{0,1}$  and  $u_{0,2}$ . These parameters, which we determine in this subsection, specify the maximum fractional deviation from the model power spectrum at  $k = 0.1 h \text{ Mpc}^{-1}$  and  $k = 0.2 h \text{ Mpc}^{-1}$ , respectively. We choose these values of  $k$  because  $k \leq 0.1$  is usually considered safely in the linear regime, while  $k = 0.2 h \text{ Mpc}^{-1}$  is the maximum wavenumber we attempt to model.

The dominant uncertainty in our model is in the relation between the power spectrum of the reconstructed halo density field and the underlying matter power spectrum, which we describe by Eqn. 14. At  $k = 0.1 h \text{ Mpc}^{-1}$  in the mock catalogues, the reconstructed halo density field and the redshift space central galaxy power spectra agree well below the percent level. The total one-halo correction  $P^{1h}$  in real space is 7-10%. If we conservatively assume that the halo reconstruction algorithm incorrectly subtracts the real space one-halo term by 20%, then the systematic error at  $k = 0.1 h \text{ Mpc}^{-1}$ ,  $u_{0,1}$ , is allowed to be 2%. At  $k = 0.2 h \text{ Mpc}^{-1}$ , the same error would translate to 5% in real space, though in redshift space this term is mitigated. In Appendix B4 we find that the shape difference of  $\hat{P}_{halo}(k)$  and  $\hat{P}_{LRG}(k)$  is only 18% at  $k = 0.2 h \text{ Mpc}^{-1}$ , and only 8% after accounting for the shot noise introduced by the fiber collision corrections. If we assume that our modeling and treatment of the one-halo contribution to the FOGs are accurate at the  $\sim 50\%$  level, we can estimate a conservative error at  $k = 0.2 h \text{ Mpc}^{-1}$  of 5%. Therefore, for all the modeling uncertainties considered so far,  $u_{0,1} = 0.02$  and  $u_{0,2} = 0.05$  encompass the estimated uncertainties.

In Appendix B2 we find that a large amount of central galaxy

misidentification or central–halo velocity bias can reduce the amplitude of  $P_{halo}(k, \mathbf{p})$  by a smoothly varying function of  $k$  at a level that exceeds these fiducial bounds on  $u_{0.1}$  and  $u_{0.2}$ . Our approach to mitigating the impact of uncertain central LRG peculiar velocities is twofold. First, for all of the analysis in Section 5 we adopt more conservative bounds for the nuisance function:  $u_{0.1} = 0.04$  and  $u_{0.2} = 0.10$ , which nearly encompass the change in power spectrum shape in Fig. B1 for the extreme velocity dispersion model. Furthermore, we calibrate a second model from the mocks with extreme velocity dispersion, and in Appendix C we determine the cosmological parameter constraints with this model to establish the level of remaining systematic uncertainty in our final results.

## 5 COSMOLOGICAL CONSTRAINTS

In this Section we explore the cosmological constraints derived from the power spectrum of the reconstructed halo density field,  $\hat{P}_{halo}(k)$ . We first consider constraints obtained from  $\hat{P}_{halo}(k)$  alone, and then combine the LRG likelihood with WMAP5 and the Union Supernova Sample (Kowalski et al. 2008) to explore joint constraints in several cosmological models. Throughout, we make use of the COSMOMC package (Lewis & Bridle 2002) to compute cosmological constraints using the Markov Chain Monte-Carlo method. A stand-alone module to compute the  $\hat{P}_{halo}(k)$  likelihood is made publicly available.<sup>2</sup>

### 5.1 Constraints from the halo power spectrum

In this subsection we examine the cosmological constraints derived from the  $\hat{P}_{halo}(k)$  alone and in combination with a prior on  $\Omega_m h^2$  from WMAP5. In the model  $P_{halo}(k, \mathbf{p})$ , the scale factor  $a_{scl}$  in Eqn. 8 is evaluated at  $z_{eff} = 0.313$ . For comparison with other works, we scale our constraint on  $D_V(0.313)$  using the fiducial distance–redshift relation, for which  $D_V(0.35)/D_V(z_{eff}) = 1.106$ ; the variation of this ratio with cosmological parameters is negligible. Following Eisenstein et al. (2005), we consider two free parameters  $\Omega_m h^2$  and  $D_V(0.35)$ . In this subsection we hold  $\Omega_b h^2 = 0.02265$ ,  $n_s = 0.960$ , and  $\sigma_8 = 0.817$  fixed at their values in the fiducial cosmological model, and assume a flat  $\Lambda$ CDM model; in §5.2 we relax these assumptions.

For the 45 bandpowers satisfying  $0.02 < k < 0.2 \text{ h Mpc}^{-1}$ ,  $\chi^2$  is minimized when  $D_V(0.35) = 1396$  and  $\Omega_m h^2 = 0.136$  with best-fitting nuisance parameters  $a_1 = 0.160$  and  $a_2 = -0.181$ ;  $\chi^2 = 39.6$  for 40 degrees of freedom. Thus the assumed model power spectrum and covariance matrix provide a reasonable fit to the observed spectrum. In a  $\Lambda$ CDM model, this point corresponds to  $h = 0.67$  and  $\Omega_m = 0.30$ . Fig 5 shows  $\chi^2$  contours in the  $\Omega_m h^2 - D_V(0.35)$  parameter space, while Table 2 reports marginalized one-dimensional constraints for several combinations of these parameters.

The information in  $\hat{P}_{halo}(k)$  can be roughly divided into broad-shape information and information from the BAO scale. Since in this subsection  $n_s$  is fixed, the shape information is the location of the turnover in the power spectrum set by matter–radiation equality, which constrains  $\Omega_m h^2 D_V$ ; information from the BAO scale constrains  $r_s/D_V$ . Here,  $r_s$  is the sound horizon at the baryon–drag epoch, which we evaluate using Eqn. 6 of Eisenstein

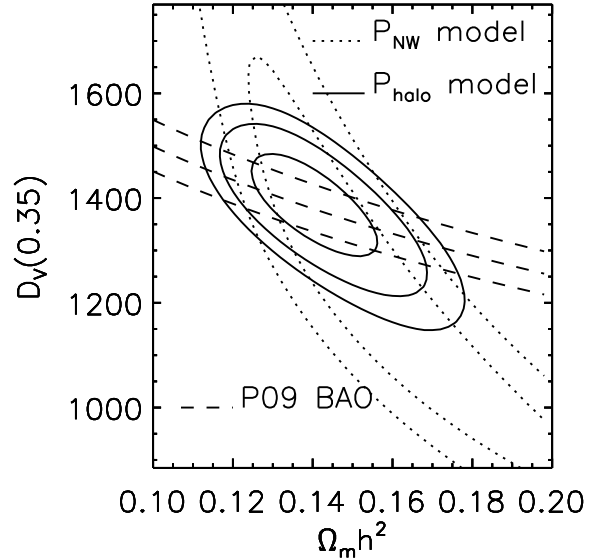


**Figure 5.** Constraints from the LRG DR7  $\hat{P}_{halo}(k)$  for a  $\Lambda$ CDM model with  $\Omega_b h^2 = 0.02265$  and  $n_s = 0.960$  fixed. The dotted contours show  $\Delta\chi^2 = 2.3$  and 6.0 contours for the  $\hat{P}_{halo}(k)$  fit to a no-wiggles model. The solid contours indicate  $\Delta\chi^2 = 2.3, 6.0$ , and 9.3 contours for  $k_{max} = 0.2 \text{ h Mpc}^{-1}$  and our fiducial  $P_{halo}(k, \mathbf{p})$  model. The three dashed lines show the best-fitting and  $\pm 1\sigma$  values  $r_s/D_V(0.35) = 0.1097 \pm 0.0036$  from P09.

& Hu (1998). These two scales correspond to constraints on  $h\Omega_m^{0.93}$  and  $h\Omega_m^{-0.37}$  respectively, in a  $\Lambda$ CDM cosmology (Tegmark et al. 2006).

To isolate information from the power spectrum turnover and exclude that of the BAO scale, we alter our model so that  $P_{damp}(k, \mathbf{p}) = P_{nw}(k, \mathbf{p})$  in Eqn. 10. The dashed lines in Fig. 5 show the constraints when using this ‘no wiggles’ model. Most of the available shape information comes from large scales with  $k < 0.1 \text{ h Mpc}^{-1}$ ; we demonstrate this in Table 2 by fitting the  $P_{damp}(k, \mathbf{p}) = P_{nw}(k, \mathbf{p})$  model with the  $\Omega_m h^2$  prior to the data up to  $k_{max} = 0.1 \text{ h Mpc}^{-1}$  and  $k_{max} = 0.2 \text{ h Mpc}^{-1}$ . The number of independent modes is proportional to  $(k_{max}^3 - k_{min}^3)$ ; thus between  $k = 0.1 \text{ h Mpc}^{-1}$  and  $k = 0.2 \text{ h Mpc}^{-1}$  there are about 7 times more modes than between  $k_{min}$  and  $0.1 \text{ h Mpc}^{-1}$ . Nevertheless, the constraint on  $\Omega_m h^2 D_V(0.35)$  only improves by  $\approx 10\%$  with the inclusion of modes between  $k_{max} = 0.1 \text{ h Mpc}^{-1}$  and  $k_{max} = 0.2 \text{ h Mpc}^{-1}$  and does not shift appreciably. This also indicates that our modeling in the quasi-linear regime  $0.1 < k < 0.2 \text{ h Mpc}^{-1}$  does not bias or substantially improve this constraint.

If we reintroduce the BAO features in the model  $P_{halo}(k, \mathbf{p})$ , then the degeneracy between  $D_V(0.35)$  and  $\Omega_m h^2$  is partially broken (solid contours in Fig. 5), and the constraints grow tighter as we include additional modes. This is understandable as the region  $0.1 < k < 0.2 \text{ h Mpc}^{-1}$  includes the location of the second BAO. The constraints on both  $r_s/D_V(0.35)$  and  $\Omega_m h^2 D_V(0.35)$  listed in Table 2 improve with  $k_{max}$ . The mean value of  $\Omega_m h^2 D_V(0.35)$  is consistent with what we find using the  $P_{damp}(k, \mathbf{p}) = P_{nw}(k, \mathbf{p})$  model with the WMAP5  $\Omega_m h^2$  prior, and does not shift substantially with increasing  $k_{max}$ . Because the BAO features break the degeneracy between  $\Omega_m h^2$  and  $D_V(0.35)$ , the LRG  $\hat{P}_{halo}(k)$  provides an independent constraint on  $\Omega_m h^2$ .

<sup>2</sup> <http://lambda.gsfc.nasa.gov/toolbox/lrgdr/>

data/model	$\Omega_m h^2$	$D_V(0.35)$ (Mpc)	$r_s/D_V(0.35)$	$\Omega_m h^2 D_V(0.35)$ (Mpc)	$A_{0.35}$
<b><math>k_{max} = 0.2</math></b>	<b><math>0.141^{+0.010}_{-0.012}</math></b>	<b><math>1380^{+61}_{-73}</math></b>	<b><math>0.1097^{+0.0039}_{-0.0042}</math></b>	<b><math>194^{+10}_{-10}</math></b>	<b><math>0.493^{+0.017}_{-0.017}</math></b>
$k_{max} = 0.15$	$0.142^{+0.010}_{-0.012}$	$1354^{+64}_{-77}$	$0.1118^{+0.0043}_{-0.0046}$	$191^{+10}_{-11}$	$0.485^{+0.018}_{-0.018}$
$k_{max} = 0.1$	$0.145^{+0.014}_{-0.016}$	$1329^{+104}_{-116}$	$0.1136^{+0.0070}_{-0.0072}$	$192^{+11}_{-12}$	$0.480^{+0.025}_{-0.024}$
$k_{max} = 0.2$ weak $F_{nuis}$	$0.139^{+0.015}_{-0.017}$	$1384^{+64}_{-77}$	$0.1099^{+0.0039}_{-0.0040}$	$192^{+17}_{-16}$	$0.490^{+0.020}_{-0.020}$
$k_{max} = 0.2$ VD	$0.148^{+0.011}_{-0.013}$	$1365^{+63}_{-76}$	$0.1096^{+0.0040}_{-0.0043}$	$202^{+10}_{-11}$	$0.499^{+0.018}_{-0.018}$
$k_{max} = 0.2$ + prior	$0.135^{+0.004}_{-0.006}$	$1411^{+44}_{-58}$	$0.1085^{+0.0036}_{-0.0036}$	$189.9^{+7.5}_{-7.5}$	$0.493^{+0.016}_{-0.016}$
$k_{max} = 0.15$ + prior	$0.135^{+0.004}_{-0.006}$	$1387^{+48}_{-61}$	$0.1104^{+0.0040}_{-0.0039}$	$186.6^{+7.9}_{-7.9}$	$0.485^{+0.017}_{-0.017}$
$k_{max} = 0.1$ + prior	$0.134^{+0.005}_{-0.007}$	$1394^{+67}_{-81}$	$0.1101^{+0.0053}_{-0.0053}$	$187.1^{+9.3}_{-9.2}$	$0.487^{+0.022}_{-0.022}$
$k_{max} = 0.2$ weak $F_{nuis}$ + prior	$0.133^{+0.005}_{-0.007}$	$1404^{+44}_{-58}$	$0.1095^{+0.0036}_{-0.0037}$	$186.1^{+8.4}_{-8.2}$	$0.487^{+0.017}_{-0.017}$
$k_{max} = 0.2$ VD + prior	$0.136^{+0.004}_{-0.006}$	$1417^{+44}_{-58}$	$0.1078^{+0.0035}_{-0.0035}$	$192.9^{+7.4}_{-7.8}$	$0.498^{+0.016}_{-0.017}$
$k_{max} = 0.1$ NW + prior	$0.134^{+0.005}_{-0.007}$	$1436^{+43}_{-50}$	$0.1076^{+0.010}_{-0.011}$	$192^{+17}_{-17}$	$0.500^{+0.047}_{-0.045}$
$k_{max} = 0.2$ NW + prior	$0.134^{+0.005}_{-0.007}$	$1463^{+134}_{-142}$	$0.1054^{+0.0092}_{-0.0095}$	$196^{+15}_{-15}$	$0.510^{+0.044}_{-0.042}$

**Table 2.** One-dimensional constraints from the LRG  $\hat{P}_{halo}(k)$  likelihood, or in combination with the WMAP5  $\Omega_m h^2$  constraint  $\Omega_m h^2 = 0.1326 \pm 0.0063$  ('+ prior', below the line). We vary the  $k_{max}$  (units of  $h \text{ Mpc}^{-1}$ ) included in the fit, the nuisance function constraints (fiducial vs weak  $F_{nuis}$ ), velocity dispersion in the model (fiducial vs. 'VD'), and whether the BAO features are included in the model (fiducial vs 'NW'). All constraints have assumed the  $\Lambda$ CDM relation between  $\Omega_m$ ,  $H_0$ , and  $D_V$ ,  $\Omega_b h^2 = 0.02265$ ,  $n_s = 0.96$ , and  $\sigma_8 = 0.817$ . In the last column we show  $A_{0.35} \equiv \sqrt{\Omega_m H_0^2 D_V(0.35)}/0.35c$  (Eisenstein et al. 2005). Models with weak  $F_{nuis}$  constraints or central galaxy velocity dispersion are discussed in Appendix C. The  $k_{max} = 0.2 h \text{ Mpc}^{-1}$  constraints highlighted in bold are our main results, and the other cases are shown for comparison.

For  $n_s = 0.96$ , we find  $\Omega_m h^2 = 0.141^{+0.010}_{-0.012}$ , which is consistent with the WMAP5 constraint,  $\Omega_m h^2 = 0.1326 \pm 0.0063$ , but with a 70% larger error.

Fig. 5 shows that the LRG-only constraints derived with  $k_{max} = 0.2 h \text{ Mpc}^{-1}$  are consistent with the intersection of the power spectrum shape constraint (dotted lines) combined with constraints on  $r_s/D_V(0.35)$  from P09: the best-fitting and  $\pm 1\sigma$  lines,  $0.1097 \pm 0.0036$  are shown as dashed lines. Note that these are one parameter  $1\sigma$  errors. Table 2 shows excellent agreement for this quantity for the LRG-only constraints, with  $r_s/D_V(0.35) = 0.1097^{+0.0039}_{-0.0042}$  for  $k_{max} = 0.2 h \text{ Mpc}^{-1}$ . This agreement reinforces the argument in Appendix A2 that our neglect of the model dependence of the window function does not introduce significant bias in the  $D_V(0.35)$  constraint. Moreover, this constraint does not change if we adopt very weak constraints on the nuisance function,  $|F_{nuis}(0.1 h \text{ Mpc}^{-1})|/b_0^2 < 0.2$  and  $|F_{nuis}(0.2 h \text{ Mpc}^{-1})|/b_0^2 < 0.5$ , or use the extreme central galaxy velocity dispersion model instead. We show in Appendix C that the largest known source of systematic uncertainty, the central galaxy velocity dispersion, impacts the cosmological parameter constraints at well below the statistical errors, and can be safely neglected for this analysis. We also demonstrate that our results are robust to the treatment of the nuisance parameters  $a_1$  and  $a_2$ .

We estimate the significance of the detection of the BAO feature as the difference between the best-fitting  $\chi^2$  for the fiducial and no wiggles models when  $a_1$ ,  $a_2$ , and  $b_0^2$  are chosen to minimize  $\chi^2$ ; we find  $\Delta\chi_{BAO}^2 = 8.9$ . The resulting constraint on  $r_s/D_V(0.35)$  is much tighter than is available from the shape information alone. To see this result, in Table 2 we combine the LRG  $\hat{P}_{halo}(k)$  likelihood with a WMAP5 prior on  $\Omega_m h^2$ . The constraint from the shape alone, obtained by fitting the no wiggles model, gives a constraint on  $r_s/D_V$  that is consistent with the constraint from the model including BAOs, but with a factor of  $\sim 2.3$  larger errors. Finally, we note that P09 estimate the total BAO detection significance to be  $\Delta\chi^2 = 13.1$ ; it is substantially larger than the value we find due to the inclusion of lower redshift galaxies from both the SDSS main sample and 2dFGRS.

Finally, Table 2 also reports our constraint on  $A_{0.35}$  (Eisenstein et al. 2005):

$$A_{0.35} \equiv \sqrt{\Omega_m H_0^2 \frac{D_V(0.35)}{0.35c}}. \quad (23)$$

This parameter is tightly constrained by the  $\hat{P}_{halo}(k)$  measurement and is independent of  $H_0$ .

## 5.2 Dependence of LRG-only constraints on the cosmological model

In Section 5.1 the cosmological parameters  $\Omega_b h^2$ ,  $n_s$ , and  $\sigma_8$  were fixed at their WMAP5 recommended values. For our purposes,  $r_s$  changes negligibly as a function of  $\Omega_b h^2$  since this parameter is so tightly constrained by CMB data. The parameters  $\Omega_m h^2$  and  $n_s$  both affect the linear power spectrum and are degenerate in shifting the contours along the constant  $r_s/D_V$  direction, as illustrated in the upper panel of Figure 6. This degeneracy is well described as  $\Omega_m h^2 (n_s/0.96)^{1.2} = 0.141$ , in good agreement with the degeneracy between these parameters found in Eisenstein et al. (2005).

In Figure 5, we have assumed the  $\Lambda$ CDM relation between  $\Omega_m$ ,  $h$ , and  $D_V$ . This determines the scale at which to apply the non-linear corrections, which are at fixed  $k$  values in units of  $h \text{ Mpc}^{-1}$ . In the bottom panel of Figure 6 we show that this assumption is not restrictive. The dashed curve fixes  $h = 0.7$  and assumes no relation between  $h$  and  $D_V$ , which also depends on  $\Omega_k$  and  $w$ . Varying  $\sigma_8$  by  $\pm 0.1$ , which enters the HALOFIT calculation of the smooth component of the non-linear matter power spectrum in Eqn. 11, changes the contours in Figure 5 negligibly.

## 5.3 Combined constraints with WMAP5 and Union SN

As probes of the redshift-distance relation, the three cosmological datasets we use in this Section are highly complementary for constraining the geometry of the universe and the equation of state of dark energy: WMAP5 effectively constrains the distance to the surface of last scatter and  $\Omega_m h^2$ , supernova data constrains angular diameter distance ratios up to  $z \sim 1$ , and  $\hat{P}_{halo}(k)$  sets joint constraints on  $r_s/D_V(0.35)$  and  $\Omega_m h^2 (n_s/0.96)^{1.2}$ . In Fig. 7 we show the intersection of these constraints for two models assuming a power law primordial power spectrum and no massive neutrinos. The blue bands indicate the WMAP5 constraints and the green

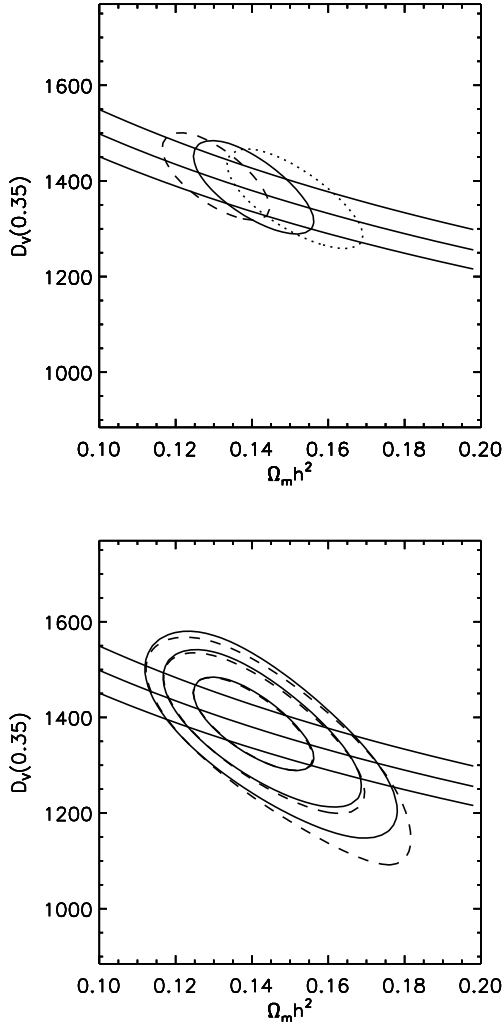


**Figure 6.** *Upper panel:* Change in  $\Delta\chi^2 = 2.3$  contour as  $n_s$  is varied, with all other parameters as in Fig. 5.  $n_s = 1.02$  (dashed),  $n_s = 0.96$  (solid), and  $n_s = 0.90$  (dotted). The degeneracy is well-described as  $\Omega_m h^2 (n_s/0.96)^{1.2} = 0.14$ . *Lower panel:* The impact of assuming a  $\Lambda$ CDM relation between  $\Omega_m$ ,  $h$ , and  $D_V$  (solid contours) compared with applying the non-linear corrections at  $h = 0.7$  and assuming no relation between  $\Omega_m$ ,  $h$ , and  $D_V(0.35)$  (dashed contours). As in Fig 5 the lines show the constraints for constant  $r_s/D_V(0.35)$  from P09.

bands show constraints using the Union Supernova Sample (Kowalski et al. 2008). For the  $\hat{P}_{halo}(k)$ , we show the constraint on  $A_{0.35}$  (open bands), which has assumed  $n_s = 0.96$  and  $\Omega_b h^2 = 0.02265$ , and is independent of  $H_0$ . In the upper panel, we have assumed  $w = -1$  and allow curvature to vary. The three independent constraints intersect near  $\Omega_m = 0.3$  and a flat universe (dashed line). In the lower panel, we assume flatness but allow  $w$  to vary; again the contours intersect near  $\Omega_m = 0.3$  and  $w = -1$ , a cosmological constant.

In this Section we combine these probes using the Markov Chain Monte Carlo (MCMC) method to obtain constraints on four cosmological models: a flat universe with a cosmological constant ( $\Lambda$ CDM), a  $\Lambda$ CDM universe with curvature (o $\Lambda$ CDM), a flat universe with a dark energy component with constant equation of state  $w$  (wCDM), and a wCDM universe with curvature (owCDM).

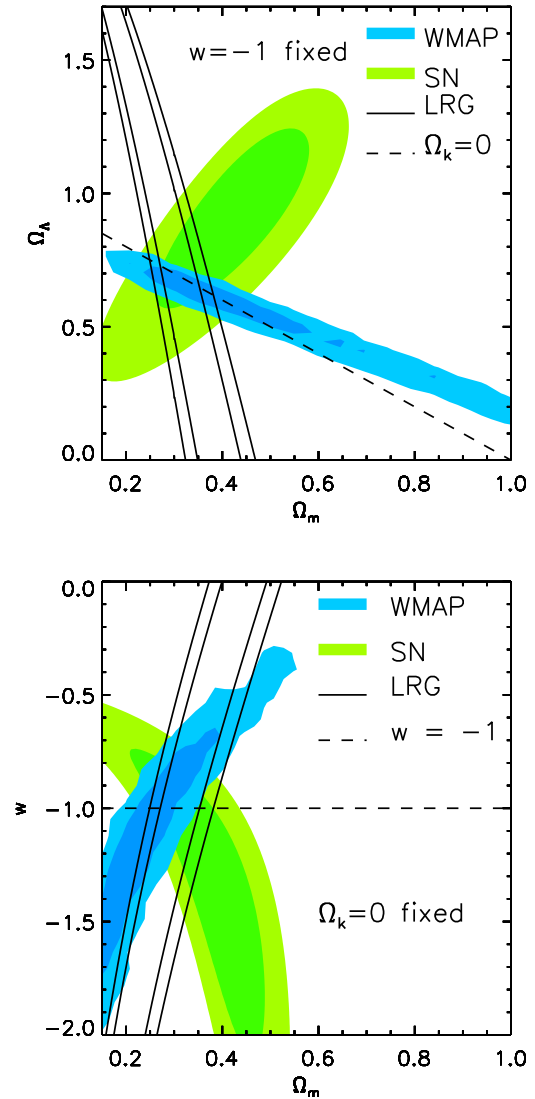


**Figure 7.** WMAP5, Union supernova sample, and the LRG  $\hat{P}_{halo}(k)$   $A_{0.35}$  constraint on the geometry of the universe. *Upper panel:* curvature varies and  $w = -1$  is fixed. The dashed line shows a flat universe,  $\Omega_m + \Omega_\Lambda = 1$ . *Lower panel:*  $w$  varies (assumed independent of redshift), and a flat universe is assumed. The dashed line indicates a cosmological constant,  $w = -1$ . WMAP5 and Union supernova contours are MCMC results, while for  $\hat{P}_{halo}(k)$ , we approximate  $\Delta\chi^2 = 2.3$  and  $\Delta\chi^2 = 6$  contours by showing  $A_{0.35} \pm \sqrt{2.3}\sigma_{A_{0.35}}$  and  $A_{0.35} \pm \sqrt{6.0}\sigma_{A_{0.35}}$  from the constraints in the top row of Table 2.

In each model we combine the constraints from  $\hat{P}_{halo}(k)$  with the WMAP5 results (Dunkley et al. 2009). In the last model, we also present constraints in combination with both WMAP5 and the Union Supernova Sample (Kowalski et al. 2008). Marginalized one-dimensional parameter constraints are presented in Table 3.

The best-fitting  $\Lambda$ CDM fit to the WMAP5+LRG likelihoods is  $(\Omega_m, \Omega_b, \Omega_\Lambda, n_s, \sigma_8, h) = (0.291, 0.0474, 0.709, 0.960, 0.820, 0.690)$  with best-fitting nuisance parameters  $a_1 = 0.172$  and  $a_2 = -0.198$ . This model has  $\chi^2_{LRG} = 40.0$  when fitting to 45 bandpowers, and is shown with the data in Fig. 8. In this model adding the information from  $\hat{P}_{halo}$  breaks the partial degeneracy between  $\Omega_m$  and  $H_0$  in the WMAP5 data and reduces the uncer-

tainties in each by a factor of  $\sim 1.6$  compared to WMAP5 alone:  $\Omega_m = 0.289 \pm 0.019$  and  $H_0 = 69.4 \pm 1.6 \text{ km s}^{-1} \text{ Mpc}^{-1}$  ( $\Omega_m = 0.258 \pm 0.03$  and  $H_0 = 71.9^{+2.6}_{-2.7} \text{ km s}^{-1} \text{ Mpc}^{-1}$  for WMAP5). The constraint on  $\sigma_8$  also tightens by 30% because of the  $\sigma_8 - \Omega_m h^2$  partial degeneracy in the WMAP5 data. Note that since we marginalize over the galaxy bias, we have no constraint on  $\sigma_8$  directly from the LRGs.

In Fig. 9 we show the effect of opening the cosmological parameter space to include curvature and a constant dark energy equation of state  $w$ . Solid contours show the  $\Lambda$ CDM constraint in each panel for comparison. The dashes show WMAP5-only constraints. Without the  $\Lambda$ CDM assumption, WMAP5 cannot constrain  $\Omega_m$  and  $H_0$  separately from  $\Omega_m h^2$ . In each of these models, the inclusion of the  $\hat{P}_{halo}(k)$  information can break the degeneracy through the BAO constraint on  $r_s/D_V$ . Table 3 shows that the cold dark matter density,  $\Omega_c h^2$ , constraint improves by  $\sim 15\%$  compared to the WMAP5-only constraint ( $\sim \pm 0.0063$ ) due to the power spectrum shape information in the non- $\Lambda$ CDM models. Moreover, the  $r_s/D_V(0.35)$  constraint does not deviate substantially from the  $\hat{P}_{halo}(k) + \Omega_m h^2$  prior constraint presented in Table 2. In the context of power-law initial conditions,  $\hat{P}_{halo}(k)$  information does not improve constraints on the spectral index  $n_s$ .

Allowing curvature relaxes the constraints on  $\Omega_m$  and  $H_0$  to the WMAP5-only  $\Lambda$ CDM errors on these parameters, while tightly constraining  $\Omega_{tot} = 1 - \Omega_k$  to  $1.0114^{+0.0077}_{-0.0076}$  ( $-0.027 < \Omega_k < 0.003$  with 95% confidence). If instead we assume flatness but allow the dark energy equation of state as an additional parameter  $w$  (assumed constant),  $w$  is constrained to  $-0.79 \pm 0.15$ . Since the effective LRG sample redshift is  $z_{eff} = 0.313$ , allowing  $w$  to deviate from  $-1$  significantly degrades the  $z = 0$  constraints,  $\Omega_m$  and  $H_0$ .

When both  $\Omega_k$  and  $w$  vary, there remains a large degeneracy between  $\Omega_m$ ,  $H_0$ , and  $w$ . Curvature is still tightly constrained and consistent with flatness at the percent level:  $\Omega_{tot} = 1.009 \pm 0.012$ . Figure 10 demonstrates that supernovae can break the degeneracy in this model. The combination of all three data sets simultaneously constrains  $\Omega_k$  within 0.009 and  $w$  to 11%, while still improving constraints on  $\Omega_m$  and  $H_0$  compared with WMAP5 alone in the  $\Lambda$ CDM model. Allowing  $\Omega_k \neq 0$  and/or  $w \neq -1$  all act to increase  $\Omega_m$  and decrease  $H_0$  compared with the  $\Lambda$ CDM model. The upper panel of Figure 10 shows that the  $\Lambda$ CDM model is only  $\sim 1\sigma$  away from the best fit. The full set of constraints on all parameters is reported in Table 3.

#### 5.4 Additional constraints from the broad $\hat{P}_{halo}(k)$ shape

For the models considered thus far, we have shown that gains in cosmological parameter constraints from adding constraints on the broad shape of  $\hat{P}_{halo}(k)$  to WMAP5 results are moderate:  $\sim 15\%$  improvement in  $\Omega_c h^2$  for all the models considered in Table 3. On the other hand, when the constraints on  $\Omega_b h^2$  and  $\Omega_c h^2$  from WMAP5 are used, our constraint on the BAO scale provides a much more precise determination of  $D_V$  at the effective redshift of the survey than the shape information alone.

In more extended models than we have thus far considered, we may expect the additional shape information to allow tighter constraints. The cosmological parameters most closely constrained by the broad  $P(k)$  shape are those which affect the shape directly or which affect parameters degenerate with the shape: these are expected to be the power spectrum spectral slope  $n_s$ , its running  $dn_s/d \ln k$ , neutrino mass  $m_\nu$ , and the number of relativis-

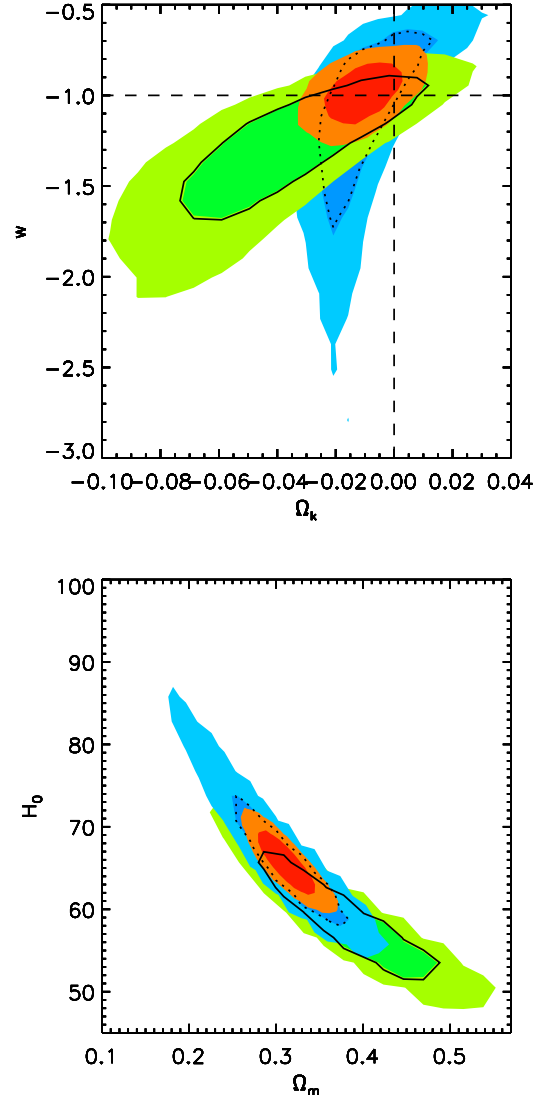


**Figure 10.** For the  $ow$ CDM model we compare the constraints from WMAP5+LRG (blue contours), WMAP5+SN (green contours), and WMAP5+LRG+SN (red contours). In the upper panel the vertical line indicates a flat universe ( $\Omega_k = 0$ ), and the horizontal line indicates a cosmological constant ( $w = -1$ ). In the both panels we overplot the WMAP5+SN 68% contour (solid black) and WMAP5+LRG (dotted black) for ease of comparison.

tic species  $N_{eff}$ . Thus far in our analysis, we have assumed  $dn_s/d \ln k = 0$ ,  $m_\nu = 0$ , and  $N_{eff} = 3.04$ .

One intuitively expects the measurement of  $\hat{P}_{halo}(k)$  to improve constraints on the primordial power spectrum. In a  $\Lambda$ CDM model where both running of the spectral index and tensors are allowed, WMAP5 still places relatively tight constraints on the primordial power spectrum:  $n_s = 1.087^{+0.072}_{-0.073}$  and  $d \ln n_s / d \ln k = -0.05 \pm 0.03$ . The measurement reported in this paper probes at most  $\Delta \ln k \sim 2$  and covers a range corresponding to  $\ell \sim 300 - 3000$ ; this range overlaps CMB measurements but extends to smaller scales. Over this  $k$ -range and for this model, WMAP5 constrains the  $P(k)$  shape to vary by  $\sim 8\%$  from variations in the primordial power spectrum. Due to the uncertainties in the relation between the galaxy and underlying matter density fields, our nuisance

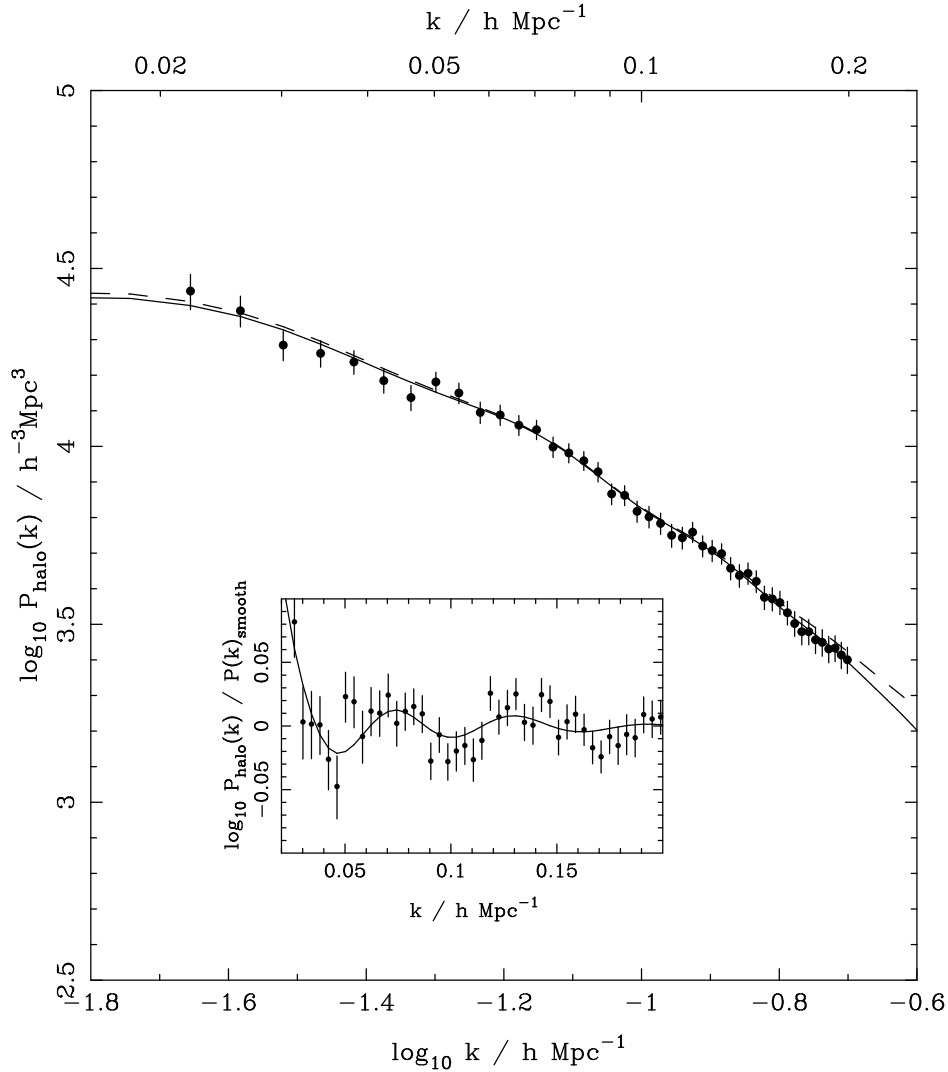


**Figure 8.** Points with errors show our measurement of  $\hat{P}_{halo}(k)$ . We show  $\sqrt{C_{ii}}$  as error bars; recall that the points are positively correlated. We plot the best-fitting WMAP5+LRG  $\Lambda$ CDM model  $(\Omega_m, \Omega_b, \Omega_\Lambda, n_s, \sigma_8, h) = (0.291, 0.0474, 0.709, 0.960, 0.820, 0.690)$  with best-fitting nuisance parameters  $a_1 = 0.172$  and  $a_2 = -0.198$  (solid curve), for which  $\chi^2 = 40.0$ ; the dashed line shows the same model but with  $a_1 = a_2 = 0$ , for which  $\chi^2 = 43.3$ . The BAO inset shows the same data and model divided by a spline fit to the smooth component,  $P_{smooth}$ , as in Fig. 4 of P09. In Section 5.1 we find the significance of the BAO detection in the  $\hat{P}_{halo}(k)$  measurement is  $\Delta\chi^2 = 8.9$ .

parameters alone allow  $P_{halo}(k, \mathbf{p})$  to vary by up to 10–14% over this region. Therefore we do not expect significant gains on  $n_s$  or  $d \ln n_s / d \ln k$  from our measurement.

The effect of massive neutrinos in the CMB power spectrum is to increase the height of the high  $\ell$  acoustic peaks: free streaming neutrinos smooth out perturbations, thus boosting acoustic oscillations. In the matter power spectrum instead, neutrino free streaming gives a scale-dependent suppression of power on the scales that large scale structure measurements currently probe (Lesgourgues & Pastor 2006). This makes these two observables highly complementary in constraining neutrino masses with cosmology.

We start by comparing the constraints from WMAP5+ $\hat{P}_{halo}(k)$  and WMAP5+BAO (using the P09 BAO likelihood) in the  $\Lambda$ CDM model with three degenerate massive neutrino species. In particular, we vary the  $\Lambda$ CDM parameters (as in Table 3) and  $\sum m_\nu$ . While WMAP5 alone finds  $\sum m_\nu < 1.3$  eV with 95% confidence, WMAP5+ $\hat{P}_{halo}(k)$  yields  $\sum m_\nu < 0.62$  eV, which is a significant improvement over

$\sum m_\nu < 0.74$  eV (WMAP5+BAO). The upper panel of Fig. 11 compares the likelihood for  $m_\nu$  for WMAP5 data alone (dashed) and in combination with  $\hat{P}_{halo}(k)$ .

A change in the number of relativistic species in the early universe changes the epoch of matter-radiation equality and thus shifts the CMB acoustic peaks. The CMB constrains the redshift of matter-radiation equality through the ratio of the third to first peak heights (Komatsu et al. 2009). If the effective number of relativistic species  $N_{eff}$  is allowed to vary, this constraint defines a degeneracy between  $\Omega_c h^2$  and  $N_{eff}$  (Dunkley et al. 2009). Note that the physical quantity that is being constrained is the physical energy density in relativistic particles. In the standard model this is given by photons and neutrinos but  $N_\nu$  should really be considered an “effective” number of relativistic neutrino species:  $N_{eff} = 3.04$  for standard neutrinos. Departures from this number can be interpreted also in terms of decay of dark matter particles, quintessence, exotic models, and additional hypothetical relativistic particles such as a light majoron or a sterile neutrino.

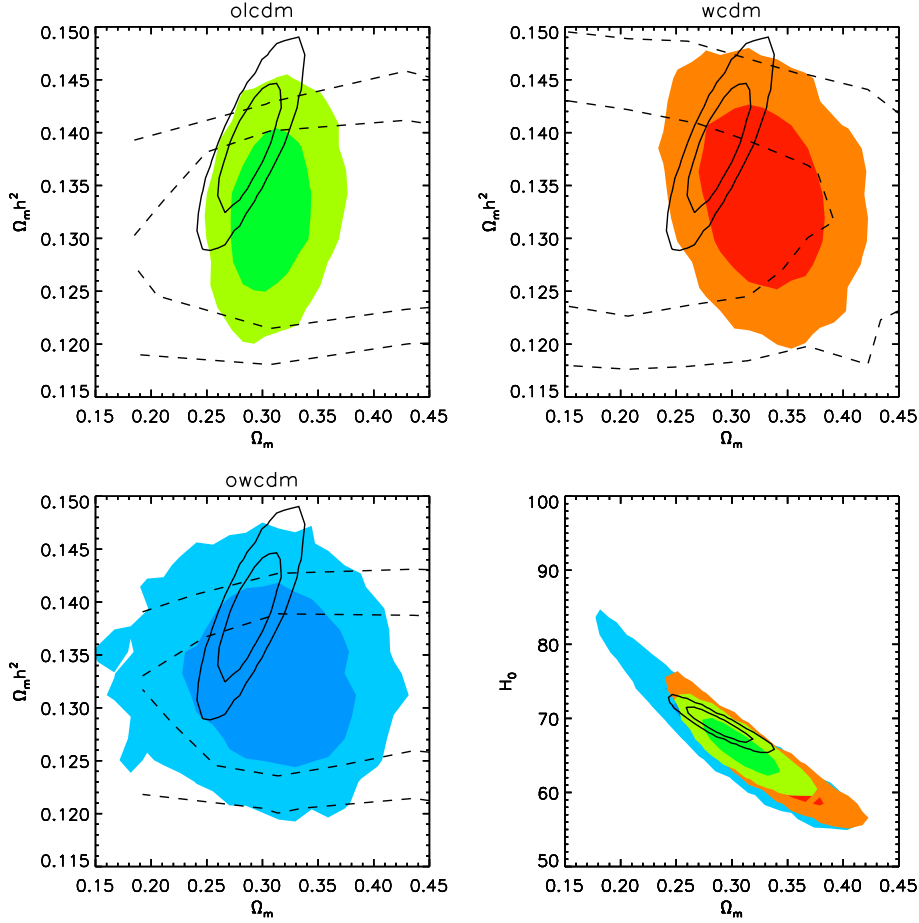


**Figure 9.** WMAP5+LRG constraints on  $\Omega_m h^2$ ,  $\Omega_m$ , and  $H_0$  for  $\Lambda$ CDM (solid black contours),  $\text{o}\Lambda$ CDM (shaded green contours),  $\text{w}\Lambda$ CDM (shaded red contours), and  $\text{ow}\Lambda$ CDM (shaded blue contours) models. The first three panels show WMAP5-only constraints (dashed contours) and WMAP5+LRG constraints (colored contours) in the  $\Omega_m h^2$ - $\Omega_m$  plane as the model is varied. In the lower right we show all constraints from WMAP5+LRG for all four models in the  $\Omega_m - h$  plane, which lie within the tight  $\Omega_m h^2 \approx 0.133$  WMAP5-only constraints.

In the  $\Lambda$ CDM model, which specifies a rigid relation between the angular diameter distance at last scattering measured by the CMB and low redshift distance scales, the degeneracy between  $N_{eff}$  and  $\Omega_c h^2$  can be broken by a low redshift constraint such as a direct measurement of  $H_0$ . However, in the  $\Lambda$ CDM model, the WMAP5 constraints on  $r_s/D_V(0.2)$  and  $r_s/D_V(0.35)$  are not altered when  $N_{eff}$  is included as a free parameter. Fig. 11 shows that the one-dimensional constraints on  $N_{eff}$  do not improve with the inclusion of the P09 BAO likelihood. However,  $N_{eff}$  will also impact the matter power spectrum, which probes the horizon size at matter-radiation equality (e.g., Eisenstein & Hu 1998). Therefore,  $\hat{P}_{halo}(k)$  is an excellent probe of  $N_{eff}$ : WMAP5+ $\hat{P}_{halo}(k)$  yields  $N_{eff} = 4.8^{+1.8}_{-1.7}$  in the  $\Lambda$ CDM model (parameters as in Table 3) with  $N_{eff}$  added as a free parameter. For comparison, Komatsu et al. (2009) find  $N_{eff} = 4.4 \pm 1.5$  when combining WMAP, BAO, supernovae, and the Hubble Space Telescope key project (Freedman et al. 2001). The lower panel of Fig. 11 compares the likelihood for  $N_{eff}$  for WMAP5 data alone with a prior  $N_{eff} \leq 10$  (dashed) and in combination with  $\hat{P}_{halo}(k)$  (solid); no prior on  $N_{eff}$  is needed in the latter case.

## 6 COMPARISON WITH OTHER ANALYSES

### 6.1 Comparison with previous galaxy clustering results

There have been several previous analyses of the clustering of the SDSS LRG spectroscopic sample. Eisenstein et al. (2005) use the correlation function of the DR3 SDSS LRG sample to derive constraints on  $\Omega_m h^2 = 0.133(n_s/0.96)^{-1.2} \pm 0.011$  and  $D_V(0.35) = 1381 \pm 64$  Mpc, where we have adjusted their constraints to match our assumed values of  $\Omega_b h^2$  and  $n_s$ ; recall that these constraints are not independent. Comparison with their Figure 7 indicates that our model is slightly more than  $1\sigma$  away from their best fit. Our analysis prefers larger  $\Omega_m h^2$  and lower  $r_s/D_V$ . In interpreting this comparison one should consider the differences in modeling and the fact that we have a factor of  $\sim 2$  larger volume. Given this larger volume, naively we would expect an improvement on the constraints by a factor of  $\sim \sqrt{2}$ . Comparison with Table 2 shows that our LRG-only constraints on  $\Omega_m h^2$  and  $D_V$  have approximately the same uncertainty as Eisenstein et al. (2005). This is partly because we conservatively increased our covariance matrix by a factor of 1.21 to account for the non-Gaussianity in the BAO contribution to the likelihood surface (see Section 2.4 discussion). However, this increase will artificially weaken the constraint from the shape. Marginalization over the two nuisance parameters

parameter	$\Lambda$ CDM	$o\Lambda$ CDM	wCDM	owCDM	owCDM+SN
$\Omega_m$	$0.289 \pm 0.019$	$0.309 \pm 0.025$	$0.328 \pm 0.037$	$0.306 \pm 0.050$	$0.312 \pm 0.022$
$H_0$	$69.4 \pm 1.6$	$66.0 \pm 2.7$	$64.3 \pm 4.1$	$66.7^{+5.9}_{-5.6}$	$65.6 \pm 2.5$
$D_V(0.35)$	$1349 \pm 23$	$1415 \pm 49$	$1398 \pm 45$	$1424 \pm 49$	$1418 \pm 49$
$r_s/D_V(0.35)$	$0.1125 \pm 0.0023$	$0.1084 \pm 0.0034$	$0.1094 \pm 0.0032$	$0.1078^{+0.0033}_{-0.0034}$	$0.1081 \pm 0.0034$
$\Omega_k$	-	$-0.0114^{+0.0076}_{-0.0077}$	-	$-0.009 \pm 0.012$	$-0.0109 \pm 0.0088$
$w$	-	-	$-0.79 \pm 0.15$	$-1.06 \pm 0.38$	$-0.99 \pm 0.11$
$\Omega_\Lambda$	$0.711 \pm 0.019$	$0.703 \pm 0.021$	$0.672 \pm 0.037$	$0.703^{+0.057}_{-0.058}$	$0.699 \pm 0.020$
Age (Gyr)	$13.73 \pm 0.13$	$14.25 \pm 0.37$	$13.87 \pm 0.17$	$14.27 \pm 0.52$	$14.24 \pm 0.40$
$\Omega_{\text{tot}}$	-	$1.0114^{+0.0077}_{-0.0076}$	-	$1.009 \pm 0.012$	$1.0109 \pm 0.0088$
$100\Omega_b h^2$	$2.272 \pm 0.058$	$2.274 \pm 0.059$	$2.293^{+0.062}_{-0.063}$	$2.279^{+0.066}_{-0.065}$	$2.276^{+0.060}_{-0.059}$
$\Omega_c h^2$	$0.1161^{+0.0039}_{-0.0038}$	$0.1110 \pm 0.0052$	$0.1112^{+0.0056}_{-0.0057}$	$0.1103^{+0.0055}_{-0.0054}$	$0.1110^{+0.0051}_{-0.0052}$
$\tau$	$0.084 \pm 0.016$	$0.089 \pm 0.017$	$0.088 \pm 0.017$	$0.088 \pm 0.017$	$0.088 \pm 0.017$
$n_s$	$0.961 \pm 0.013$	$0.962 \pm 0.014$	$0.969 \pm 0.015$	$0.965 \pm 0.016$	$0.964 \pm 0.014$
$\ln(10^{10} A_{05})$	$3.080^{+0.036}_{-0.037}$	$3.068 \pm 0.040$	$3.071^{+0.040}_{-0.039}$	$3.064 \pm 0.041$	$3.068 \pm 0.039$
$\sigma_8$	$0.824 \pm 0.025$	$0.796 \pm 0.032$	$0.735 \pm 0.073$	$0.79 \pm 0.11$	$0.790^{+0.045}_{-0.046}$

**Table 3.** Marginalized one-dimensional constraints (68%) for WMAP5+LRG for flat  $\Lambda$ CDM,  $\Lambda$ CDM with curvature ( $o\Lambda$ CDM), flat wCDM (wCDM), wCDM with curvature (owCDM), and wCDM with curvature and including constraints from the Union Supernova sample. Here  $\tau$  is the optical depth to reionization,  $n_s$  is the scalar spectral index, and  $A_{05}$  is the amplitude of curvature perturbations at  $k = 0.05/\text{Mpc}$ ; these parameters are constrained directly by the CMB only. We place uniform priors on the parameters varied in the MCMC chains, with the exception of  $A_{SZ}$ : ( $\Omega_b h^2$ ,  $\Omega_c h^2$ ,  $\theta$ ,  $n_s$ ,  $\ln(10^{10} A_{05})$ ,  $\tau$ ,  $A_{SZ}$ ).  $\theta$  is the approximate angular diameter distance to recombination (standard in the COSMOMC package) and  $A_{SZ}$  is the amplitude of the SZ power spectrum contribution. We use the hard prior  $0 < A_{SZ} < 2$  as in the WMAP5 analysis. Where constraints are presented,  $\Omega_k$  and  $w$  are also varied; other parameters listed have been derived from this complete set. In all models in this table, we have also assumed the standard contribution from  $N_{eff} = 3.04$  massless neutrino species to the relativistic energy density. We relax these assumptions about neutrinos in Section 5.4.

$a_1$  and  $a_2$  to account for our uncertainty in the  $P_{halo}(k, \mathbf{p})$  as well as our conservative cut at  $k_{min}$  also slightly weaken the constraint from the power spectrum shape.

Tegmark et al. (2006) report cosmological constraints from a somewhat larger LRG sample (SDSS DR4) and combine their results with WMAP3 data. To compare LRG-only constraints, we use the value derived from the Tegmark et al. (2006) power spectrum in Sánchez & Cole (2008):  $\Omega_m h = 0.173 \pm 0.017$  for  $n_s = 1.0$  and  $h = 0.72$ . For a  $\Lambda$ CDM model scaled to  $n_s = 1.0$ , our LRG-only constraints yield  $\Omega_m h = 0.200^{+0.012}_{-0.011}$ . Restricting our analysis to  $k_{max} = 0.1 h \text{ Mpc}^{-1}$  to match Tegmark et al. (2006), we find  $\Omega_m h = 0.195 \pm 0.013$ . Besides the increase in sample volume, the discrepancy between these results could be due to differences in the FOG compression and the degeneracy between their nuisance parameter  $Q$  (see Eqn. 1) and cosmological parameters. A detailed comparison of our modeling approaches is given in Reid et al. (2009). Note that Sanchez et al. (2009) have also recently completed an analysis of the LRG correlation function, but they do not present a constraint from their shape measurement with which we can compare.

Our results agree with analyses of photometric LRG samples. Padmanabhan et al. (2007) find  $\Omega_m = 0.30 \pm 0.03$  for  $h = 0.7$  and  $n_s = 1$ , and Blake et al. (2007) find  $\Omega_m h = 0.195 \pm 0.023$  for  $h = 0.75$  and  $n_s = 1$ . Our constraint is also consistent with determinations from other galaxy samples. For the 2dFGRS sample, Cole et al. (2005) find  $\Omega_m h = 0.168 \pm 0.016$  for fixed  $n_s = 1.0$  and  $h = 0.72$ ; allowing a 10% Gaussian uncertainty in  $h$  yields  $\Omega_m h = 0.174 \pm 0.019$ , which is within  $1\sigma$  of our LRG-only constraint. Our results are also in good agreement with the SDSS main sample: Tegmark et al. (2004b) find  $\Omega_m h = 0.201 \pm 0.017$ , again with fixed  $n_s = 1.0$  and  $h = 0.72$ .

## 6.2 Comparison with P09

The P09 constraints overlap significantly with our analysis. We showed in Section 5.1 that our LRG-only constraint on

$r_s/D_V(0.35)$  is in very good agreement with the determination in P09. When combined with the WMAP5 constraint on  $\Omega_m h^2$  (lower portion of Table 2), our use of the shape information in  $\hat{P}_{halo}(k)$  allows  $\sim 10\%$  improvement on  $r_s/D_V(0.35)$ . Moreover, the shape information provides a tighter constraint on  $\Omega_c h^2$ . However, the P09 inclusion of SDSS main and 2dFGRS galaxies allows an additional constraint on  $r_s/D_V(0.2)$ , which generally makes the P09 constraints on  $\Omega_m$  and  $H_0$  tighter. Our constraints on  $\Omega_k$  and  $w$  are comparable to P09. Across the models we have studied, WMAP5+ $\hat{P}_{halo}(k)$  constraints yield lower values of  $H_0$  than the P09 results. This is driven by the P09  $r_s/D_V(0.2)$  constraint, which pulls the overall distance scale slightly lower compared to  $r_s/D_V(0.35)$  alone, but does not signal any inconsistency between these analyses. Also note that the correlation function analysis of the DR7 LRG sample by Kazin et al. (2009) shows good agreement with the power spectrum analysis in P09.

## 6.3 Comparison with Riess et al. (2009) $H_0$

Riess et al. (2009) recently released a new determination of the Hubble constant using a differential distance ladder:  $H_0 = 74.2 \pm 3.6 \text{ km s}^{-1} \text{ Mpc}^{-1}$ . This value is consistent at the  $\sim 1\sigma$  level with the WMAP5+ $\hat{P}_{halo}(k)$  result for the  $\Lambda$ CDM model,  $H_0 = 69.4 \pm 1.6 \text{ km s}^{-1} \text{ Mpc}^{-1}$ . Table 3 shows that if we allow  $\Omega_k \neq 0$  and/or  $w \neq -1$ , the mean value of  $H_0$  decreases to  $\sim 64 - 67 \text{ km s}^{-1} \text{ Mpc}^{-1}$ . Therefore, combining the Riess et al. (2009) measurement with our constraints should reduce the uncertainties further and push the best-fitting model closer to  $\Lambda$ CDM. P09 present constraints including the Riess et al. (2009)  $H_0$  constraint for the owCDM model; the impact should be similar when using  $\hat{P}_{halo}(k)$  rather than the P09 BAO constraints.

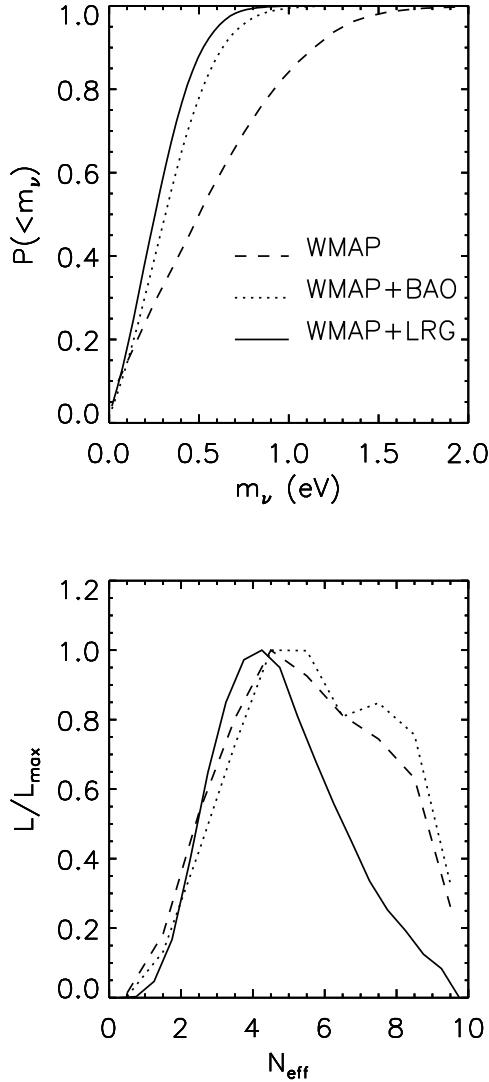


**Figure 11.**  $\hat{P}_{halo}(k)$  improves constraints on neutrinos in the  $\Lambda$ CDM model through both the BAO scale and the broad power spectrum shape constraints. We show the one dimensional cumulative probability for WMAP alone (dashed), WMAP+P09 BAO (dotted), and WMAP+ $\hat{P}_{halo}(k)$  (solid) for the neutrino mass (upper panel) and the one dimensional likelihood for the effective number of relativistic species  $N_{eff}$  (lower panel). The decrease at large  $N_{rel}$  for the WMAP and WMAP+BAO constraints are a result of the hard prior  $N_{eff} \leq 10$ .

## 7 CONCLUSIONS

In this paper we have presented the power spectrum of the reconstructed halo density field derived from a sample of Luminous Red Galaxies (LRGs) from the Sloan Digital Sky Survey DR7. The size of LRG DR7 sample has sufficient statistical power that the details of the relation between LRGs and the underlying linear density field become important and need to be reliably modeled before attempting a cosmological interpretation of the data. Here, we have adopted the method of Reid et al. (2009), which applies a pre-processing step to the measured galaxy density field to reconstruct the halo density field before computing the halo power spectrum. On the scales of interest, this power spectrum has a more direct and

robust connection to the underlying linear, real space power spectrum than the power spectrum of the LRG galaxies themselves.

We calibrate our method using  $N$ -body simulations with volume and resolution suitably tuned to trace the halo mass range relevant to LRGs, and provide several consistency checks between the observed and mock galaxy density fields to support our approach to model the LRG sample’s clustering properties. In particular, we demonstrate the validity of our modeling of the small-scale clustering and FOG features by matching the observed and mock catalogue higher-order statistics probed by the Counts-in-Cylinders group multiplicity function as well as the relative line of sight velocities between galaxies occupying the same halo. We discuss and quantify the sources of systematic error remaining in our modeling. For the LRG sample, with  $\bar{n}P \sim 1$ , both the shot noise subtraction and the large velocity dispersions of their host haloes can introduce uncertainty. We identify the largest source of systematic uncertainty to be the velocity dispersion of central LRGs within their host haloes, and find its effects on cosmological parameters to be safely smaller than the size of the statistical errors. We are able to derive quantitative bounds on our model uncertainties and propagate these through the cosmological analysis by introducing nuisance parameters with tightly controlled allowed ranges, based on our understanding of the sources of non-linearity in the spectrum.

Based on our modeling of the LRG sample, we are able to extend our model for  $\hat{P}_{halo}(k)$  to  $k = 0.2 h \text{ Mpc}^{-1}$ , increasing the number of available modes by a factor of  $\sim 8$  over an analysis restricted to  $k_{max} = 0.1 h \text{ Mpc}^{-1}$ , as was the case in the SDSS team’s DR4 analysis (Tegmark et al. 2006). This allows us to simultaneously constrain the broadband shape of the underlying linear power spectrum and detect the BAO signal with  $\Delta\chi^2 = 8.9$ , though most of the shape information is confined to  $k < 0.1 h \text{ Mpc}^{-1}$ .

If we fix  $n_s$  and  $\Omega_b h^2$ ,  $\hat{P}_{halo}(k)$  alone constrains both  $\Omega_m h^2 = 0.141^{+0.010}_{-0.012}$  and  $D_V(0.35) = 1380^{+60}_{-73}$ . The agreement of our constraint on  $\Omega_m h^2$  at  $z_{eff} \sim 0.31$  with the one derived from the CMB at  $z \sim 1000$  provides a remarkable consistency check for the standard cosmological model. When  $\hat{P}_{halo}(k)$  is combined with WMAP5, the error on  $\Omega_c h^2$  is reduced by  $\sim 15\%$ , and the constraint on  $D_V(0.35)$  allows us to place tight constraints on both  $\Omega_m$  and  $H_0$ , as well as  $\Omega_k$  or  $w$ . If we also include the Union Supernova Sample, all four parameters can be tightly constrained:  $\Omega_m = 0.312 \pm 0.022$ ,  $H_0 = 65.6 \pm 2.5 \text{ km s}^{-1} \text{ Mpc}^{-1}$ ,  $\Omega_k = -0.0109 \pm 0.008$ , and  $w = -0.99 \pm 0.11$ , which is consistent with  $\Lambda$ CDM at the  $\sim 1\sigma$  level. In fact, in the spirit of Occam’s razor, these constraints can be taken as evidence against both  $\Omega_k \neq 0$  and  $w \neq -1$ , since their values must conspire to match the observed angular diameter distance at recombination as well as  $D_V(0.35)$ ; this can be seen from Fig. 7.

Finally, we show that the shape information in  $\hat{P}_{halo}(k)$  can improve constraints on both massive neutrinos and the number of relativistic species  $N_{eff}$  in a  $\Lambda$ CDM model. In combination with WMAP5 we find  $\sum m_\nu < 0.62 \text{ eV}$  at the 95% confidence level and  $N_{eff} = 4.8^{+1.8}_{-1.7}$ . These represent 16% (30%) improvements over using the WMAP5+BAO likelihood from P09.

This paper represents a first attempt to analyse the LRG redshift survey with a model that accounts for the non-linear galaxy bias and non-linear redshift space distortions introduced by the so-called one-halo term, and to propagate the uncertainty in the modeling through the cosmological constraints. We expect that the technique introduced here to estimate the halo density field will be useful to further refinements such as reconstruction of the baryon

acoustic peak (Eisenstein et al. 2007a) and measurement of  $\beta$  from redshift space distortions. The modeling efforts presented in this paper are rather specific to the SDSS LRG sample. However, similar techniques to probe the relation between the galaxy and underlying matter density fields as well as to quantify its uncertainty will be required in the analysis of larger data sets from future galaxy surveys.

## ACKNOWLEDGEMENTS

BAR gratefully acknowledges support from NSF Grant OISE/0530095 and FP7-PEOPLE-2007-4-3-IRG while this work was being completed, and thanks Raul Jimenez for useful discussions and computing power. WJP is grateful for support from the UK Science and Technology Facilities Council, the Leverhulme trust and the European Research Council. LV acknowledges support from FP7-PEOPLE-2007-4-3-IRG n 20218 and MICINN grant AYA2008- 03531. DNS acknowledges NSF grants AST-0707731 and OISE05-30095. DJE was supported by National Science Foundation grant AST-0707225 and NASA grant NNX07AC51G. Simulated catalogues were calculated and analysed using the COSMOS Altix 3700 supercomputer, a UK-CCC facility supported by HEFCE and STFC in cooperation with CGI/Intel. We acknowledge the use of the Legacy Archive for Microwave Background Data Analysis (LAMBDA). Support for LAMBDA is provided by the NASA Office of Space Science. We also acknowledge the use of the CAMB, CMBFAST, CosmoMC, and WMAP5 likelihood codes.

Funding for the SDSS and SDSS-II has been provided by the Alfred P. Sloan Foundation, the Participating Institutions, the National Science Foundation, the U.S. Department of Energy, the National Aeronautics and Space Administration, the Japanese Monbukagakusho, the Max Planck Society, and the Higher Education Funding Council for England. The SDSS Web Site is <http://www.sdss.org/>.

The SDSS is managed by the Astrophysical Research Consortium for the Participating Institutions. The Participating Institutions are the American Museum of Natural History, Astrophysical Institute Potsdam, University of Basel, Cambridge University, Case Western Reserve University, University of Chicago, Drexel University, Fermilab, the Institute for Advanced Study, the Japan Participation Group, Johns Hopkins University, the Joint Institute for Nuclear Astrophysics, the Kavli Institute for Particle Astrophysics and Cosmology, the Korean Scientist Group, the Chinese Academy of Sciences (LAMOST), Los Alamos National Laboratory, the Max-Planck-Institute for Astronomy (MPIA), the Max-Planck-Institute for Astrophysics (MPA), New Mexico State University, Ohio State University, University of Pittsburgh, University of Portsmouth, Princeton University, the United States Naval Observatory, and the University of Washington.

## REFERENCES

- Abazajian, K., et al. 2009, *ApJ Suppl.*, 182, 543  
 Adelman-McCarthy, J. K., et al. 2006, *ApJ Suppl.*, 162, 38  
 Bardeen, J. M., Bond, J. R., Kaiser, N., & Szalay, A. S. 1986, *ApJ*, 304, 15  
 Blake, C., Collister, A., Bridle, S., & Lahav, O. 2007, *MNRAS*, 374, 1527  
 Blanton, M. R., Lin, H., Lupton, R. H., Maley, F. M., Young, N., Zehavi, I., & Loveday, J. 2003, *Astron. J.*, 125, 2276  
 Blanton M.R., et al., 2003b, *ApJ*, 592, 819  
 Carlson, J., White, M., & Padmanabhan, N. 2009, arXiv:0905.0479  
 Cole, S., & Kaiser, N. 1989, *MNRAS*, 237, 1127  
 Cole, S., et al. 2005, *MNRAS*, 362, 505  
 Coles P., Jones B., 1991, *MNRAS*, 248, 1  
 Colless, M., Dalton, G., Maddox, S., Sutherland, W., Norberg, P., Cole, S., et al. 2001, *MNRAS*, 328, 1039  
 Colless, M., et al. 2003, arXiv:astro-ph/0306581  
 Cooray, A., & Sheth, R. 2002, *Physics Reports*, 372, 1  
 Coziol, R., Andernach, H., Caretta, C. A., Alamo-Martínez, K. A., & Tago, E. 2009, *Astron. J.*, 137, 4795  
 Cresswell, J. G., & Percival, W. J. 2009, *MNRAS*, 392, 682  
 Davis, M., Groth, E. J., & Peebles, P. J. E. 1977, *ApJ Lett.*, 212, L107  
 Davis, M., & Peebles, P. J. E. 1977, *ApJ Suppl.*, 34, 425  
 —. 1983, *ApJ*, 267, 465  
 Dunkley, J., et al. 2009, *ApJ Suppl.*, 180, 306  
 Eisenstein, D. J., et al. 2001, *Astron. J.*, 122, 2267  
 Eisenstein, D. J., & Hu, W. 1998, *ApJ*, 496, 605  
 Eisenstein, D. J., Seo, H.-J., Sirko, E., & Spergel, D. N. 2007a, *ApJ*, 664, 675  
 Eisenstein, D. J., Seo, H.-J., & White, M. 2007b, *ApJ*, 664, 660  
 Eisenstein, D. J., et al. 2005, *ApJ*, 633, 560  
 Feldman, H. A., Kaiser, N., & Peacock, J. A. 1994, *ApJ*, 426, 23  
 Freedman, W. L., et al. 2001, *ApJ*, 553, 47  
 Fukugita, M., Ichikawa, T., Gunn, J. E., Doi, M., Shimasaku, K., & Schneider, D. P. 1996, *Astron. J.*, 111, 1748  
 Górski, K.M., Hivon E., Banday A.J., Wandelt B.D., Hansen F.K., Reinecke M., Bartelmann M., 2005, *ApJ*, 622, 759  
 Gott, J. R., Choi, Y.-Y., Park, C. & Kim, J., *ApJ Lett.*, 695, 45  
 Gramann, M., Cen, R., & Gott, J. R. I. 1994, *ApJ*, 425, 382  
 Gunn, J. E., et al. 1998, *Astron. J.*, 116, 3040  
 Gunn, J. E., et al. 2006, *Astron. J.*, 131, 2332  
 Hamilton, A. J. S. 1998, in *Astrophysics and Space Science Library*, Vol. 231, *The Evolving Universe*, ed. D. Hamilton, 185–+  
 Hamilton, A. J. S., Rimes, C. D., & Scoccimarro, R. 2006, *MNRAS*, 371, 1188  
 Hatton, S., & Cole, S. 1999, *MNRAS*, 310, 1137  
 Heitmann, K., White, M., Wagner, C., Habib, S., & Higdon, D. 2008, arXiv:0812.1052  
 Ho, S., Lin, Y.-T., Spergel, D., & Hirata, C. M. 2009, *ApJ*, 697, 1358  
 Hockney R.W., Eastwood J.W., 1988, *Computer simulation using particles*, New York: McGraw-Hill  
 Hogg, D. W., Finkbeiner, D. P., Schlegel, D. J., & Gunn, J. E. 2001, *Astron. J.*, 122, 2129  
 Ivezić, Ž., et al. 2004, *Astronomische Nachrichten*, 325, 583  
 Kaiser, N. 1984, *ApJ Lett.*, 284, L9  
 —. 1987, *MNRAS*, 227, 1  
 Kazin, E. et al. 2009, arXiv:0908.2598  
 Komatsu, E., et al. 2009, *ApJ Suppl.*, 180, 330  
 Kowalski, M., et al. 2008, *ApJ*, 686, 749  
 Kulkarni, G. V., Nichol, R. C., Sheth, R. K., Seo, H.-J., Eisenstein, D. J., & Gray, A. 2007, *MNRAS*, 378, 1196  
 Lesgourgues, J., & Pastor, S. 2006, *Physics Reports*, 429, 307  
 Lewis, A., & Bridle, S. 2002, *Phys. Rev. D*, 66, 103511  
 Lewis, A., Challinor, A., & Lasenby, A. 2000, *ApJ*, 538, 473  
 Lin, Y.-T., & Mohr, J. J. 2004, *ApJ*, 617, 879

- Lunnan, R., Gott, J. R., Park, C. & Kim, J. prep, ArXiv Astrophysics e-prints
- Mandelbaum, R., Seljak, U., Kauffmann, G., Hirata, C. M., & Brinkmann, J. 2006, MNRAS, 368, 715
- Masjedi, M., Hogg, D. W., Cool, R. J., Eisenstein, D. J., Blanton, M. R., Zehavi, I., Berlind, A. A., Bell, E. F., Schneider, D. P., Warren, M. S., & Brinkmann, J. 2006, ApJ, 644, 54
- Matsubara, T. 2008, Phys. Rev. D, 78, 083519
- Mo, H. J., & White, S. D. M. 1996, MNRAS, 282, 347
- Nolta, M. R., et al. 2009, ApJ Suppl., 180, 296
- Padmanabhan, N., et al. 2008, ApJ, 674, 1217
- Padmanabhan, N., et al. 2007, MNRAS, 378, 852
- Page, L., et al. 2003, ApJ Suppl., 148, 39
- Peacock, J. A., & Dodds, S. J. 1994, MNRAS, 267, 1020
- Peacock, J. A., & Smith, R. E. 2000, MNRAS, 318, 1144
- Percival, W. J., et al. 2001, MNRAS, 327, 1297
- Percival, W. J., et al. 2007, ApJ, 657, 645
- Percival, W. J., Verde, L., & Peacock, J. A. 2004, MNRAS, 347, 645
- Percival, W. J., et al. prep, ArXiv Astrophysics e-prints
- Perlmutter, S. & The Supernova Cosmology Project. 1999, ApJ, 517, 565
- Pier, J. R., Munn, J. A., Hindsley, R. B., Hennessy, G. S., Kent, S. M., Lupton, R. H., & Ivezić, Ž. 2003, Astron. J., 125, 1559
- Press W.H., Teukolsky S.A., Vetterling W.T., Flannery B.P., 1992, Numerical recipes in C. The art of scientific computing, Second edition, Cambridge: University Press.
- Rees, M. J. 1985, MNRAS, 213, 75P
- Reid, B. A., & Spergel, D. N. 2009, ApJ, 698, 143
- Reid, B. A., Spergel, D. N., & Bode, P. 2009, ApJ, 702, 249
- Riess, A. G., et al. 1998, Astron. J., 116, 1009
- Riess, A. G., et al. 2009, ApJ, 699, 539
- Sánchez, A. G., & Cole, S. 2008, MNRAS, 385, 830
- Sanchez, A. G., Crocce, M., Cabre, A., Baugh, C. M., & Gaztanaga, E. 2009, arXiv:0901.2570
- Saunders, W., et al. 2000, MNRAS, 317, 55
- Scherrer, R., & Weinberg, D. 1998, ApJ, 504, 607
- Schlegel, D., White, M., & Eisenstein, D. 2009, arXiv:0902.4680
- Seljak, U. 2001, MNRAS, 325, 1359
- Skibba, R., van den Bosch, F. C., Yang, X., & Mo, H. J. prep, ArXiv Astrophysics e-prints
- Smith, J. A., et al. 2002, Astron. J., 123, 2121
- Smith, R. E., Peacock, J. A., Jenkins, A., White, S. D. M., Frenk, C. S., Pearce, F. R., Thomas, P. A., Efstathiou, G., & Couchman, H. M. P. 2003, MNRAS, 341, 1311
- Smith, R. E., Scoccimarro, R., & Sheth, R. K. 2007, Phys. Rev. D, 75, 063512
- Spergel, D. N., et al. 2003, ApJ Suppl., 148, 175
- Stoughton, C., et al. 2002, Astron. J., 123, 485
- Strauss, M., et al. 2002, Astron. J., 124, 1810
- Tegmark, M. 1997, Phys. Rev. D, 56, 4514
- Tegmark, M., et al. 2004a, ApJ, 606, 702
- . 2004b, ApJ, 606, 702
- Tegmark, M., et al. 2006, Phys. Rev. D, 74, 123507
- Tegmark, M., et al. 2004, Phys. Rev., D69, 103501
- Tucker, D. L., et al. 2006, Astronomische Nachrichten, 327, 821
- van den Bosch, F. C., Weinmann, S. M., Yang, X., Mo, H. J., Li, C., & Jing, Y. P. 2005, MNRAS, 361, 1203
- van den Bosch, F. C., Yang, X., Mo, H. J., Weinmann, S. M., Macciò, A. V., More, S., Cacciato, M., Skibba, R., & Kang, X. 2007, MNRAS, 376, 841
- Verde, L., & Peiris, H. 2008, JCAP, 7, 9
- Wake, D. A., et al. 2008, MNRAS, 387, 1045
- Yang, X., Mo, H. J., van den Bosch, F. C., Pasquali, A., Li, C., & Barden, M. 2007, ApJ, 671, 153
- Yoo, J., Weinberg, D. H., Tinker, J. L., Zheng, Z., & Warren, M. S. 2009, ApJ, 698, 967
- York, D. G., et al. 2000, Astron. J., 120, 1579
- Zehavi, I., et al. 2005a, ApJ, 621, 22
- Zehavi, I., et al., 2005b, ApJ, 630, 1
- Zel'dovich, Y. B. 1970, Astron. Astrophys., 5, 84
- Zheng, Z., et al. 2005, ApJ, 633, 791
- Zheng, Z., Zehavi, I., Eisenstein, D. J., Weinberg, D. H., & Jing, Y. 2008, arXiv:0809.1868

## APPENDIX A: TESTING MODEL APPROXIMATIONS

In this Appendix we present tests to demonstrate the validity of several assumptions of our model  $P_{halo}(k, \mathbf{p})$ .

### A1 Isotropy tests

Both our  $P_{halo}(k, \mathbf{p})$  model (Eqn. 16) and the  $a_{sci}$  approximation (Eqn. 8) assume that the power spectrum modes are distributed isotropically with respect to the line of sight. We check this assumption in the SDSS DR7 LRG galaxy sample using pairs of galaxies separated by  $\Delta r_{min} = 15 h^{-1}$  Mpc to  $\Delta r_{max} = 150 h^{-1}$  Mpc, binned into nine equal bins in  $\Delta r$  of width  $15 h^{-1}$  Mpc. We consider the angles between the galaxy pair separation vector and the local line of sight vector defined between the observer and each of the galaxies in the pair. These two angles will be equal in the limit of a pair with  $\Delta r \ll \max(\chi_1, \chi_2)$  where  $\chi_1$  and  $\chi_2$  are the distances to the two galaxies and  $\Delta r$  is the separation between them. We find  $\langle \cos^2 \phi \rangle - 0.333$  is  $-0.01$  for the smallest separation bin ( $15 h^{-1}$  Mpc  $< \Delta r < 30 h^{-1}$  Mpc) and  $+0.005$  in the largest separation bin. Figure A1 shows the full distribution versus  $|\cos \phi|$ . The small increase for pairs perpendicular to the line of sight for the smallest separation bin is due to non-linear redshift space distortions (FOGs), inducing a potentially large separation in redshift space between nearby pairs of galaxies in real space. The few percent deviations from isotropy will induce negligible variations in the shape of the angle-averaged  $P_{halo}(k, \mathbf{p})$ , since the lower left panel of Figure 7 in Reid et al. (2009) indicates only a  $\sim 5\%$  change to the power spectrum shape between real and redshift space at  $k = 0.2 h \text{ Mpc}^{-1}$ .

### A2 $D_V$ approximation

As in Section 3.4, we use the approximation that pairs of galaxies contributing to  $\hat{P}_{halo}(k)$  in the  $k$ -range of interest are located at the same redshift to compute the effective survey redshift:

$$z_{eff} = \frac{\int z n^2(z) \frac{w^2(z)}{b^2(z)} \frac{dV}{dz} dz}{\int n^2(z) \frac{w^2(z)}{b^2(z)} \frac{dV}{dz} dz}, \quad (\text{A1})$$

where  $n(z)$ ,  $b(z)$ , and  $w(z)$  specify the average number density, bias, and weight of the sample at redshift  $z$  as defined in Percival et al. (2004). We find  $z_{eff} = 0.313$ , and use this redshift to evaluate  $a_{sci}$  in Eqn. 8. The effective redshift changes by only  $\Delta z = 0.004$  if one instead weights by the expected number of galaxies at redshift  $z$ . Given the distribution of pairs in the small

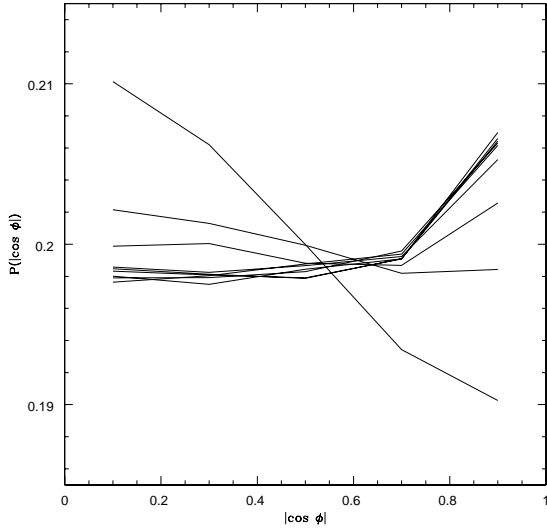


**Figure A1.**  $P(|\cos \phi|)$  vs  $\cos \phi$  where  $\phi$  is the angle between the galaxy pair separation vector and the line of sight defined by the observer and one of the galaxies in the pair (see text). The smallest separation bin ( $15 h^{-1}$  Mpc  $< \Delta r < 30 h^{-1}$  Mpc) shows the largest deviation from isotropy, with a  $\sim 5\%$  preference for pairs perpendicular to the line of sight compared to along the line of sight due to FOGs. The larger separation bins extend to  $150 h^{-1}$  Mpc and are nearly isotropic, but with a few percent excess of pairs directly along the line of sight.

separation limit (Eqn. 19) we estimate the fractional bias remaining after the correction in Eqn. 8 is applied as

$$\frac{\delta D_V}{D_V} \approx \frac{\int \left( \frac{D_V(z)}{D_V(z_{eff})} \frac{D_V^{\text{fiducial}}(z_{eff})}{D_V^{\text{fiducial}}(z)} - 1 \right) n^2(z) \frac{w^2(z)}{b^2(z)} \frac{dV}{dz} dz}{\int n^2(z) \frac{w^2(z)}{b^2(z)} \frac{dV}{dz} dz} \quad (\text{A2})$$

For a  $\Lambda$ CDM model, the fractional bias on the distance scale is  $< 0.1\%$  in the range  $\Omega_m = 0.2 - 0.4$  and the rms change is  $< 1.2\%$ . This additional variance about the peak is negligible for the BAO scale  $\sim 100 h^{-1}$  Mpc since this is much smaller than the damping scale  $\sigma_{BAO} \sim 9 h^{-1}$  Mpc. We find very similar results for the bias and rms damping if we instead integrate over the full distribution of isotropic pairs instead of using the  $D_V$  approximation in Eqn. A2.

Testing this approximation in more general models is more subtle, since  $D_V(z)$  depends on  $H_0$ ,  $\Omega_m$ ,  $\Omega_k$ , and  $w$ . We instead do a consistency check: for  $\Omega_m h^2$  constrained by WMAP5,  $D_V(z_{eff})$  constrained by WMAP5+ $\hat{P}_{halo}(k)$ ,  $\Omega_k = 0$ , and  $-2 < w < -0.5$ , the maximum fractional bias is  $\sim 0.5\%$ , and the maximum rms change is 3.5%; a similar analysis for  $-0.025 < \Omega_k < 0.025$  and  $w = -1$  shows much smaller deviations. We therefore conclude that in the range of models considered here, a single scale factor  $a_{sci}$  can accurately account for the effects of the model redshift distance relation on the interpretation of the measured power spectrum.

### A3 Comparing $P_{nw}$ approximations

In the models without massive neutrinos, we have used the Eisenstein & Hu (1998) formula (Eqn. 29) to compute  $P_{nw}$ , which enters our model in Eqn. 10. However, for more general models such as those containing massive neutrinos or which vary the number of relativistic species, it is more convenient to use a spline to ob-

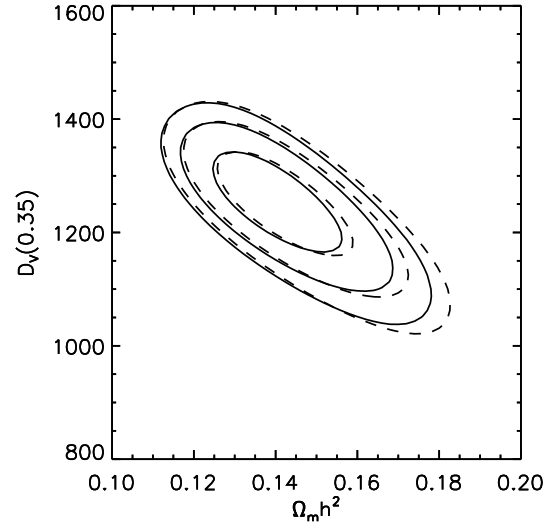


**Figure A2.** Comparison of the LRG-only likelihood surface computed with the analytic approximation of  $P_{nw}$  in Eqn. 29 of Eisenstein & Hu (1998) (solid, as in Fig. 5) compared with the result when using the b-spline fit described in Appendix A3 (dashed).

tain a smooth version of  $P_{lin}$  without BAO features. We fit a cubic b-spline to  $P_{lin} k^{1.5}$  in order to minimize the slope in the  $k$  region of interest. There are eight equally spaced nodes starting at  $k = 0.0175 \text{ Mpc}^{-1}$  and ending at  $k = 0.262 \text{ Mpc}^{-1}$ , and an additional node at  $k = 0.0007 \text{ Mpc}^{-1}$ . Note we fix the location of the nodes in units of  $\text{Mpc}^{-1}$  since the linear power spectrum is fixed in those units for fixed  $\Omega_m h^2$  and  $\Omega_b h^2$ . Fig. A2 shows that the LRG-only likelihood surfaces computed with these two approximations agree well in the region preferred by WMAP5:  $\Omega_m h^2 = 0.133 \pm 0.0063$ .

## APPENDIX B: QUANTIFYING MODEL UNCERTAINTIES AND CHECKS FOR SYSTEMATICS: DETAILS

In this Appendix we aim to quantify the sources of systematic uncertainty in the model  $P_{halo}(k)$ . The model is calibrated on the mock catalogues of Reid et al. (2009). In Appendix B1 and Appendix B2 we present the detailed assumptions we have made to produce the mock catalogues from the  $N$ -body simulation halo catalogues, and discuss the expected impact of these assumptions on the predicted relation between the reconstructed halo and matter density fields. Appendix B3 through B6 present consistency checks between the observed and mock catalogue LRG density fields that address the modeling uncertainties. In Section 4.3, the results of these tests are used to establish quantitative bounds on the nuisance parameters in Eqn. 15 to be used in our cosmological parameter analysis.

### B1 Halo model parametrization

In Reid et al. (2009) we adopt the following parametrization for the average number of LRGs in a halo of mass  $M$  (Zheng et al. 2005):

$$\langle N(M) \rangle = \langle N_{cen} \rangle (1 + \langle N_{sat} \rangle) \quad (\text{B1})$$

$$\langle N_{cen} \rangle = \frac{1}{2} \left[ 1 + \text{erf} \left( \frac{\log_{10} M - \log_{10} M_{min}}{\sigma_{\log M}} \right) \right] \quad (\text{B2})$$

$$\langle N_{sat} \rangle = \left( \frac{M - M_{cut}}{M_1} \right)^\alpha. \quad (\text{B3})$$

For our adopted fiducial cosmological model, we find  $\sigma_{\log M} \sim 0.6-0.9$  in order to match the amplitude of the observed large scale clustering of the LRGs; the exact parameter values used to generate the mock catalogues are given in Reid et al. (2009). Since the scale dependence of halo bias varies with halo mass at the  $\sim 10\%$  level at  $k = 0.15 h \text{ Mpc}^{-1}$  (Smith et al. 2007), changes in the distribution of LRGs with halo mass that preserve the large scale clustering amplitude could result in few percent changes in non-linear bias of the haloes traced by the LRGs. Changes in the distribution of halo biases traced by the LRGs could also alter the relation between the CiC and true group multiplicity function, which would introduce further uncertainty in the relation between the reconstructed and underlying halo density fields.

## B2 Distribution of mock galaxies within haloes

In the mock catalogues of Reid et al. (2009) used to calibrate our model  $P_{halo}(k, \mathbf{p})$ , we have assumed a sharp distinction between ‘central’ and ‘satellite’ galaxies. The first or ‘central’ LRG in each halo is assumed to sit at the halo centre and move with the mean velocity of the halo dark matter; roughly 94% of the LRGs in our sample are central galaxies (Zheng et al. 2008; Reid et al. 2009). For the  $\sim 6\%$  of LRGs that are ‘satellites’, we assume that they trace the phase space distribution of the halo dark matter, so that their positions and velocities are assigned to be that of a random dark matter particle in the halo.

We do not evaluate the impact of errors in our assumed real space distribution of galaxies in their haloes on the fidelity of the halo density field reconstruction; the impact will be negligible in the case where there is a single LRG per halo. However, if the observed galaxies have a significantly different real space distribution in their haloes than we have assumed, the relationship between the reconstructed halo density field and underlying matter density field will be different in the observed and mock galaxy catalogues. We test our assumed spatial distribution in Appendix B3 by checking for consistency between the observed and mock catalogues for CiC group multiplicity functions, measured with two distinct sets of cylinder parameters. Furthermore, we can use Eqn. 21 (where the measured CiC group multiplicity function specifies  $\langle N_{gal}(N_{gal} - 1) \rangle$ ) as an upper limit on the error on the shot noise term due to differences between the model and observed reconstructed halo density fields.

We consider two possible sources of deviation from our assumed galaxy distribution within haloes. The first is that on occasion an isolated LRG in our sample is not the ‘central’ galaxy in its halo, but a satellite galaxy, while the ‘central’ galaxy in that halo is not selected by our sample cuts. We call this situation ‘central misidentification’, and denote its probability  $f_{cen, err}$ , assumed independent of halo mass for simplicity. The brightest LRGs are indeed centrally concentrated, with  $\sim 80\%$  of them within  $\sim 0.2 r_{vir}$  of the X-ray peak (Ho et al. 2009). Lin & Mohr (2004) similarly find that 80% of the BCGs in their X-ray selected cluster sample are within  $\sim 0.1 r_{vir}$ , and in the  $\sim 8\%$  of cases where the BCG is outside  $0.5 r_{vir}$ , the second ranking galaxy in the group is within  $0.1 r_{vir}$ . In some of these cases, both the first and second brightest galaxies would be identified as LRGs; van den Bosch et al. (2007) showed that the luminosity difference between first and second brightest galaxies in massive groups is typically small. In this situation there would be no error in our catalogues since we are not assigning luminosities to our mock LRGs. From these studies

we would expect  $f_{cen, err} < 0.2$  for the halo mass scales probed by these studies,  $M > 10^{14} M_\odot$ , and it is reasonable to assume this holds at lower masses where there are fewer massive galaxies per halo. We therefore choose  $f_{cen, err} = 0.2$  as our ‘optimistic’ value in the cases we consider in Fig. B1. Using a galaxy group and cluster catalogue from SDSS (Yang et al. 2007), Skibba et al. (prep) find that the fraction of clusters in which the central galaxy is fainter than the brightest satellite is  $\approx 30\%$  in the mass range  $M \sim 10^{13} - 10^{14} M_\odot$  and  $\approx 40\%$  for  $M \sim 10^{14} - 10^{15} M_\odot$ . It is not clear what these results imply for the LRG galaxy sample, but the parameter  $f_{cen, err}$  aims to encompass this case. We choose  $f_{cen, err} = 0.4$  as our ‘conservative’ estimate for the cases we consider in Fig. B1.

The second situation we consider is the breakdown of our assumption that the central galaxy has no peculiar motion with respect to the mean velocity of the halo dark matter. Any offset with respect to the halo centre implies that central galaxies are moving with respect to the halo centre (van den Bosch et al. 2005; Skibba et al. prep). We call this situation central–halo velocity bias and parametrize the amplitude as  $b_{vel}^2 = \sigma_{cen}^2 / \sigma_{DM}^2$ , the ratio of the mean square velocity of the central galaxy to the halo dark matter. Skibba et al. (prep) find  $b_{vel} \sim 0.1$  once central misidentification has been accounted for. This small value is negligible for our purposes, so we set  $b_{vel} = 0$  in the ‘optimistic’ and ‘conservative’ cases we consider in Fig. B1. However, Coziol et al. (2009) find  $b_{vel} \sim 0.3$  for brightest cluster members. This quantity is difficult to extract from observations, and it is not clear how the literature results apply to the LRG sample because of the color-magnitude cuts defining the LRG selection. We set  $b_{vel} = 0.6$  in the ‘extreme’ case we consider in Fig. B1.

On the large scales of interest, the effect of nonzero  $f_{cen, err}$  or  $b_{vel}$  is to give the mock galaxies a velocity with respect to the halo centre. In Figure B1 we show the impact of nonzero central galaxy velocities on the recovered  $P_{halo}(k, \mathbf{p})$  for the three cases we described above. In the ‘optimistic’ case, we set  $(f_{cen, err}, b_{vel}) = (0.2, 0)$ ; in the ‘conservative’ case, we set  $(f_{cen, err}, b_{vel}) = (0.4, 0)$ ; and in the ‘extreme’ case, we set  $(f_{cen, err}, b_{vel}) = (0.2, 0.6)$ . To construct mock catalogues in each of these cases we leave the real space distribution of galaxies fixed. To mimic central misidentification, we replace the central galaxy’s velocity with the velocity of a randomly selected dark matter particle halo member. For central–halo velocity bias, we replace the central galaxy velocity with  $b_{vel} v_{ran}$ , where  $v_{ran}$  is the velocity of a randomly selected dark matter particle halo member. For comparison, we also outline both our fiducial nuisance function constraints (2% deviation at  $k = 0.1 h \text{ Mpc}^{-1}$  and 5% at  $k = 0.2 h \text{ Mpc}^{-1}$ ) and the conservative nuisance function constraints (4% deviation at  $k = 0.1 h \text{ Mpc}^{-1}$  and 10% at  $k = 0.2 h \text{ Mpc}^{-1}$ ) established in Section 4.3. The ‘optimistic’ case is well within the fiducial nuisance constraints, and the ‘conservative’ case is well within the conservative nuisance constraints. The ‘extreme’ case, however, exceeds the conservative nuisance constraints for  $k > 0.17 h \text{ Mpc}^{-1}$ . In Section 5 we also evaluate the cosmological parameter constraints when  $P_{halo}(k, \mathbf{p})$  is calibrated using the power spectrum of the ‘extreme’ velocity dispersion model in order to derive a limit on the systematic errors on our final results.

## B3 Comparison of mock and observed CiC group statistics

In Table B1 we present CiC group multiplicity functions normalized by the number of galaxies per sample for two sets of cylinder parameters:  $\Delta r_\perp \leq 0.8 h^{-1} \text{ Mpc}$ ,  $\Delta v_p = 1800 \text{ km s}^{-1}$  (these

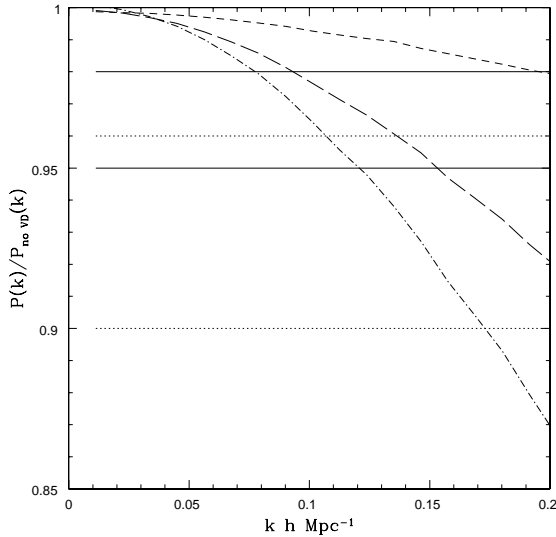


**Figure B1.** We compare three models including central galaxy velocity dispersion to our fiducial model with no central galaxy velocity dispersion ( $f_{cen,err} = b_{vel} = 0$ ) by showing the ratio of  $P_{halo}(k, \mathbf{p}_{fid})$  for the models. The dashed curve has  $f_{cen,err} = 0.2, b_{vel} = 0$  (‘optimistic’); the long dashed curve has  $f_{cen,err} = 0.4, b_{vel} = 0$  (‘conservative’); the dash-dot curve has  $f_{cen,err} = 0.2, b_{vel} = 0.6$  (‘extreme’). The straight lines show our fiducial (solid) and conservative (dotted) nuisance parameter constraints determined in Section 4.3.

are the parameters used to define our CiC groups and reconstructed halo density field for  $P_{halo}(k, \mathbf{p}_{fid})$  and  $\Delta r_{\perp} \leq 1.2 h^{-1}$  Mpc,  $\Delta v_p = 1800 \text{ km s}^{-1}$ . The second CiC multiplicity function computed with larger  $\Delta r_{\perp}$  is used to demonstrate consistency between the mock and observed catalogues. If the observed satellite galaxies were significantly less concentrated than in our mock catalogues, we would detect these galaxies when  $\Delta r_{\perp}$  is increased.

The observed groups contain 2158 LRGs that were assigned redshifts by the fiber collision correction. According to Reid & Spergel (2009), where colors are used as a redshift indicator, up to  $\sim 36\%$  of these may be erroneous assignments; correcting this would remove  $\sim 780$  galaxies from the observed groups. We find 6.2% of the observed galaxies are ‘satellite’ galaxies using the reconstructed haloes, or 5.5% if we apply a correction for erroneous fiber collision assignments, while our mock catalogues have 5.9%. The structures of the multiplicity functions are generally similar. Since our mock catalogues were designed to match this measurement but for LRGs selected as in Zehavi et al. (2005), the level of agreement is as expected. We verify that the agreement extends to the multiplicity function when we adjust the group finding parameter  $\Delta r_{\perp}$  to be 50% larger. Accounting for the possible contamination from fiber collision corrections, which is likely to manifest mostly at  $n_{group} = 2$ , we see that in general the observed distribution is smaller than in the mock catalogues at all multiplicities and for both values of  $\Delta r_{\perp}$ . This result may be understood as one or more of three possibilities: the mocks having too many satellites altogether, different amounts of contamination from interlopers due to errors in the small-scale two-halo redshift space correlation function, or a tighter distribution of satellite galaxies about the central one in the mocks. An error of the first kind would result in no error in the reconstructed density field; errors of the other kinds would result in small changes to the effective shot noise or FOG features in the density field. The last line in Table B1 shows that

$n_{group}$	$N_{CiC,obs}(n)$	$N_{CiC,mock}(n)$	$N_{big,obs}(n)$	$N_{big,mock}(n)$
2	5283	4717	6432	6280
3	539	658	899	1076
4	110	124	198	252
5	26	28.2	39	71.4
6	7	7.68	27	22.9
7	1	2.32	5	8.65
8	3	0.78	5	3.34
9	0	0.30	0	1.39
10	0	0.10	0	0.66
$P^{1h} \bar{n}_{gal}$	0.144	0.143	0.205	0.225

**Table B1.** The observed and mock catalogue CiC group multiplicity functions of groups with  $n_{group}$  galaxies for our fiducial group finding parameters  $\Delta r_{\perp,max} = 0.8 h^{-1}$  Mpc,  $\Delta v_p = 1800 \text{ km s}^{-1}$  and for a bigger  $\Delta r_{\perp,max} = 1.2 h^{-1}$  Mpc. The final row shows the ratio of the one-halo shot noise  $P_{LRG}^{1h}$  (Eqn. 21) to the standard shot noise correction  $1/n_{LRG}$ .

the difference in the effective one halo term derived from the mock and observed catalogues using Eqn. 21 is  $< 2\%$  of the total shot noise correction. Since the difference between  $P^{1h} \bar{n}_{gal}$  measured at  $\Delta r_{\perp} \leq 0.8 h^{-1}$  Mpc and  $\Delta r_{\perp} \leq 1.2 h^{-1}$  Mpc is less for the observed catalogues compared with the mocks, we cannot be missing significant contributions to  $P^{1h}$  due to a less concentrated distribution of the satellite galaxies in the observed haloes compared with the simulated ones; rather, the increase in the number of groups comes from the increase in contamination from galaxies residing in nearby haloes. Our final conservative nuisance parameter bounds, discussed in Section 4.3, allow an error of the order of 40% in the one-halo shot noise subtraction. Also note that because the maximum line of sight separation ( $\Delta v_p = 1800 \text{ km s}^{-1}$  or  $\sim 20 h^{-1}$  Mpc) is so large, the model CiC multiplicity functions are nearly identical when we consider the model with ‘extreme’ central galaxy velocity dispersion. Finally, adding some spatial dispersion of the central galaxies would slightly reduce the number of CiC groups for an otherwise fixed catalogue; this may bring the models and observations into even closer agreement.

We compute the line of sight separation of galaxies in the same CiC group as a probe of the accuracy of our model galaxy velocities at the high halo mass end, where there is more than one LRG per halo. The comparison is complicated by the presence of fiber collision corrected galaxies, since their redshifts are artificially set to that of another galaxy in their group. We discard all such groups, and discard an equal fraction at each  $n_{group}$  in our mock sample. The resulting distributions are shown in Fig. B2. The fiducial mocks with no central galaxy velocity dispersion appear to fit the data better, though neither matches the observed sharpness of the rise at small separations. Note that the fiducial mock catalogues with no velocity dispersion are determined only by the observed  $N_{CiC}(n_{group})$ ; no free parameters have been adjusted to match the observed velocity distribution. This comparison indicates that the residual FOG features in the reconstructed observed and mock halo density fields will be in satisfactory agreement.

#### B4 Comparison of $\hat{P}_{halo}(k)$ and $\hat{P}_{LRG}(k)$

In this subsection we examine the difference between the observed redshift space monopole spectrum  $\hat{P}_{LRG}(k)$  (no density field preprocessing of FOG features) and the power spectrum of the reconstructed halo density field,  $\hat{P}_{halo}(k)$ , and compare with our mock galaxy catalogues. This comparison provides an additional consistency check between the mock and observed LRG catalogues, and

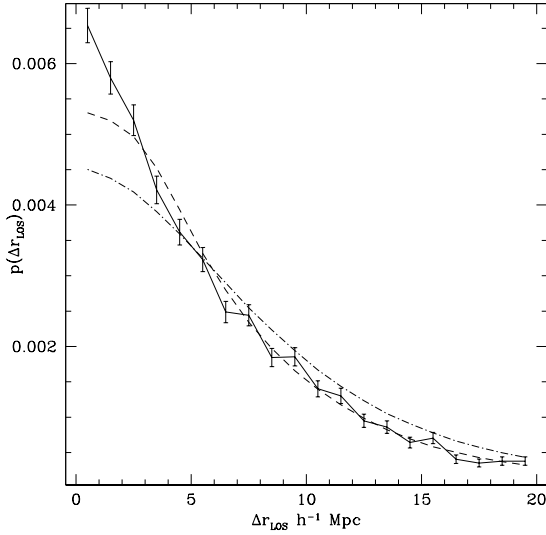


**Figure B2.** Solid line with error bars is the observed probability that a galaxy has a member of its CiC group with a separation  $\Delta r_{LOS}$  along the line of sight for pairs of galaxies identified as pairs by the CiC criteria, once all groups containing a fiber collision galaxy are removed. Error bars indicate fractional errors of  $1/\sqrt{N}(\Delta r_{LOS})$ , giving a sense of the Poisson level of uncertainty in the measurement without considering the contribution from cosmic variance. The dashed line is the expected distribution for our model with no central galaxy velocity dispersion, and the dot-dashed line is for the model with central galaxy velocity dispersion. Note that  $\Delta r_{LOS} = 1 h^{-1} \text{ Mpc}$  corresponds to  $\Delta v \approx 115 \text{ km s}^{-1}$  for the redshift distribution of our sample.

quantifies the effect of the halo density field reconstruction step on the measured power spectrum shape.

We consider

$$\Delta P(k) = P_{LRG}(k) - b_{rel}^2 P_{halo}(k) \quad (\text{B4})$$

where  $b_{rel}$  is a constant that parametrizes the enhancement of the overall bias when satellite galaxies are included, since they occupy the most highly biased regions. In real space on large scales,  $\Delta P(k)$  would be a simple shot noise, but in redshift space we expect the detailed  $\Delta P(k)$  to result from the transfer of power between scales caused by the FOGs, making  $\Delta P(k)$  dependent on the underlying power spectrum shape. We will ignore this possible  $< 10\%$  level modification to the expected  $\Delta P(k)$  since we have demonstrated good agreement between the shape of the mock and observed halo power spectra. The lower short dashed curve in Fig. B3 shows the predicted  $\Delta P(k)$  from our mock catalogues, the upper short dashed curve shows the predicted  $\Delta P(k)$  scaled by a factor of 1.5, and the solid curve shows  $\Delta P(k)$  for the observed spectra. The observed  $\Delta P(k)$  is clearly flatter as a function of  $k$  than the shape expected from our mock catalogues (dashed curves).

A crucial difference between the observed and mock LRG density fields is the application of fiber collision corrections discussed in Section 2.1 in the observed density field. 2158 galaxies without spectra were added to the LRG sample and assigned the redshift of the nearest LRG, while the CiC group multiplicity results in Table B1 indicate that 6857 galaxies are ‘satellite’ galaxies. First, since  $\sim 36\%$  of the fiber-collision corrections are erroneous (Reid & Spergel 2009), we expect an additional shot noise of  $\sim 125(h^{-1} \text{ Mpc})^3$  from these galaxies (Eqn. 21), which are not represented in our mock catalogues. Second, the fiber collision

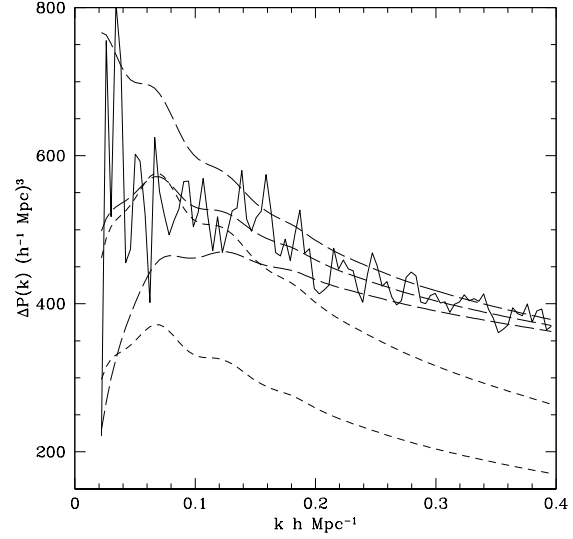


**Figure B3.** The solid curve is the difference between the observed spectra  $\hat{P}_{halo}(k)$  and  $\hat{P}_{LRG}(k)$ , the lower short-dashed curve is the predicted difference from our simulated catalogues, and the upper short-dashed curve is the same curve but scaled by a factor of 1.5. The scale dependence of  $\Delta P(k)$  is smaller for the observed spectra than for the simulation results. Furthermore, there is some uncertainty in the appropriate value of  $b_{rel}$ , which changes the shape of  $\Delta P(k)$ . However, at high  $k$ , the prediction is robust to changes in  $b_{rel}$  since  $P(k)$  is small. The long-dashed curves show  $\Delta P_{mock}(k) + 200(h^{-1} \text{ Mpc})^3$  for several values of  $b_{rel}$ . This demonstrates that the difference between  $\hat{P}_{halo}(k)$  and  $\hat{P}_{LRG}(k)$  is consistent with the difference measured in the simulated catalogues if the excess shot noise from fiber collisions is accounted for. Moreover, the difference between the observed halo and LRG spectra is large compared with the statistical errors on the bandpowers.

corrected galaxies that are physically associated with a neighboring LRG will change the distribution of  $\Delta P(k)$  relative to the mocks because their line of sight separation from the neighboring galaxy has been eliminated. The long dashed curves in Fig. B3 shows that we can match the observed  $\Delta P(k)$  as a sum of the mock catalogue  $\Delta P(k)$  and a shot noise of  $200(h^{-1} \text{ Mpc})^3$ . The  $\Delta P(k)$  for the observed spectra is consistent with a constant power for  $k < 0.2 h \text{ Mpc}^{-1}$  and amounts to a significant difference between the two spectra:  $\sim 8\%$  at  $k = 0.1 h \text{ Mpc}^{-1}$  and  $\sim 18\%$  at  $k = 0.2 h \text{ Mpc}^{-1}$ . Therefore, differences in the preprocessing of the LRG density field can lead to changes in  $P(k)$  much larger than the statistical errors on the measurements, which could then be propagated to errors in the derived cosmological parameters. Note that the reconstructed halo density field is basically unaffected by errors in the close-pair fiber collision correction applied to the data, since these galaxies are all assigned to haloes containing other LRGs already.

In summary, the difference between  $\hat{P}_{halo}(k)$  and  $\hat{P}_{LRG}(k)$  can be understood once we account for the effects of fiber collisions, and the model predictions  $P_{halo}(k, \mathbf{p})$  are robust to any uncertainty associated with these effects.

## B5 The effect of luminosity-weighting on $\hat{P}_{halo}(k)$

A further subtle difference between the mock and observed halo power spectrum is that the mock catalogues were evaluated using a redshift snapshot with constant  $\bar{n}_{LRG}$ , and luminosities were not

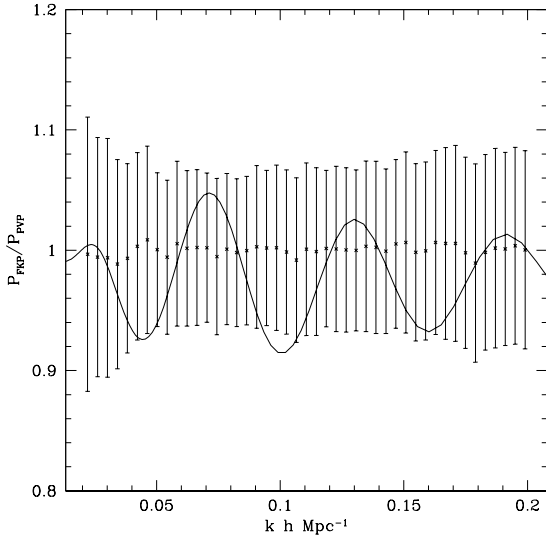


**Figure B4.** Ratio of the power spectra computed using the weights in Eqn. B6 to the standard Percival et al. (2004) weighting scheme after rescaling the overall normalization. We also overplot  $P_{lin}(k)/P_{nw}(k)$  for our fiducial model to demonstrate no correlation between the small shifts in the measured power spectrum and expected BAO feature. Errors show the fractional errors on  $\hat{P}_{halo}(k)$ ,  $\sqrt{C_{ii}}/\hat{P}_{halo}(k)$ .

assigned to the mock LRGs; each reconstructed halo is weighted equally when computing the overdensity field. To verify that the luminosity weighting used to compute the  $\hat{P}_{halo}(k)$  does not significantly alter the relative amplitude of the shot noise to total power compared with our mock catalogues, we recompute  $\hat{P}_{halo}(k)$  from the data with luminosity-independent weights from Feldman et al. (1994):

$$b(L) = 1 \quad (\text{B5})$$

$$w(r, L) = \frac{1}{1 + P_o \bar{n}_{LRG}} \quad (\text{B6})$$

where  $P_o = 10000(h^{-1} \text{ Mpc})^3$ . Fig. B4 shows the ratio of the observed spectra with our fiducial weights compared with the luminosity-independent weights. The good agreement even at large  $k$  where the power is small indicates there is no significant difference from the shot noise subtraction between these two weightings; we find no statistically significant change in the power spectrum shape. Moreover, the change in the windowed theory power spectrum due to the change in weights is negligible ( $< 0.1\%$ ), indicating that the window function will not be sensitive to the particular weighting choices of Section 2 for reconstructed haloes containing more than one galaxy. While the luminosity-weighting is critical for the SDSS main sample (Tegmark et al. 2004b), Fig. 1 shows that the LRGs are close to volume-limited over much of the redshift range of the sample; it is therefore unsurprising that the Feldman et al. (1994) and Percival et al. (2004) weighting schemes produce nearly identical power spectra for the LRG sample.

## B6 Checking the cosmological dependence of the model

Our model uses HALOFIT to describe the cosmological parameter dependence of the non-linearity in the matter power spectrum, and is calibrated from  $N$ -body simulations at the fiducial cosmology (Eqn. 13). Below  $k = 0.1 h \text{ Mpc}^{-1}$ , the dark matter power spec-

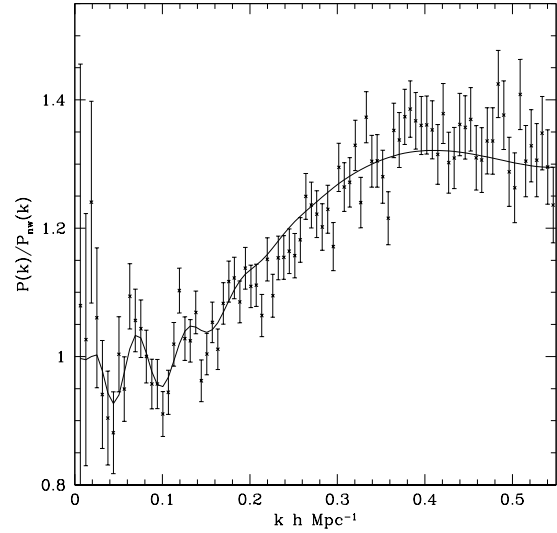


**Figure B5.** Agreement between  $P_{halo, WMAP3}(k)/P_{nw}(k, \mathbf{p}_{WMAP3})$  measured from the catalogues in Reid & Spergel (2009) based on an  $N$ -body simulation  $z = 0.2$  snapshot with WMAP3 cosmological parameters (points with error bars) vs. the model prediction from Eqn 16 at  $z_{NEAR} = 0.235$ .

trum is linear at the 1% level, apart from the BAO damping, and it is only  $\sim 15\%$  larger than the linear one at  $k = 0.2 h \text{ Mpc}^{-1}$ . Using the publicly available WMAP5  $\Lambda$ CDM MCMC chain, we find  $P_{halofit}(k)/P_{lin}(k)$  changes by  $\sim \pm 2\%$  for  $k \leq 0.2$  in the space of cosmologies allowed by the WMAP5 data alone; the error on this small correction will therefore be well below 1%. Therefore we expect the model of the non-linear matter power spectrum to be accurate at the  $< 1\%$  level at  $k = 0.1 h \text{ Mpc}^{-1}$  and  $\sim 1\%$  at  $k = 0.2 h \text{ Mpc}^{-1}$ .

We use the LRG catalogues from Reid & Spergel (2009) evaluated at the WMAP3 preferred cosmological parameters  $(\Omega_m, \Omega_b, \Omega_\Lambda, n_s, \sigma_8, h) = (0.26, 0.044, 0.74, 0.95, 0.77, 0.72)$  at  $z = 0.2$  with  $L_{box} = 1 h^{-1} \text{ Gpc}$  to test the cosmological dependence of our model  $P_{halo}(k, \mathbf{p})$  in Eqn. 13. We plot a mock catalogue power spectrum  $P_{halo, WMAP3}(k)/P_{nw}(k, \mathbf{p}_{WMAP3})$  against our  $P_{halo}(k, \mathbf{p})$  model predictions for a NEAR subsample in Fig. B5 to demonstrate the agreement both in the BAO features and overall shape of the deviation out to  $k = 0.55 h \text{ Mpc}^{-1}$ .  $\chi^2 = 96.6$  for 86 DOF ( $k \leq 0.55$ ) and  $\chi^2 = 29.1$  for 31 DOF ( $k \leq 0.2$ ). This provides further evidence that the cosmological dependence of our model  $P_{halo}(k, \mathbf{p})$  is sufficiently accurate for the SDSS DR7 data, which probe a somewhat smaller volume.

## APPENDIX C: EFFECTS OF CENTRAL GALAXY VELOCITY DISPERSION AND NUISANCE PARAMETERS

In Section 4 we established that the largest remaining known source of systematic uncertainty is the central galaxy velocity dispersion. To test the impact of this uncertainty on the cosmological constraints, we reevaluate the  $\hat{P}_{halo}(k)$  likelihood surface using the ‘extreme’ velocity dispersion model in Appendix B2 to calibrate the model  $P_{halo}(k, \mathbf{p})$ . The maximum likelihood points for the fiducial, no velocity dispersion model (cross) and the ‘extreme’ velocity dispersion model (‘X’) are shown in the upper left panel

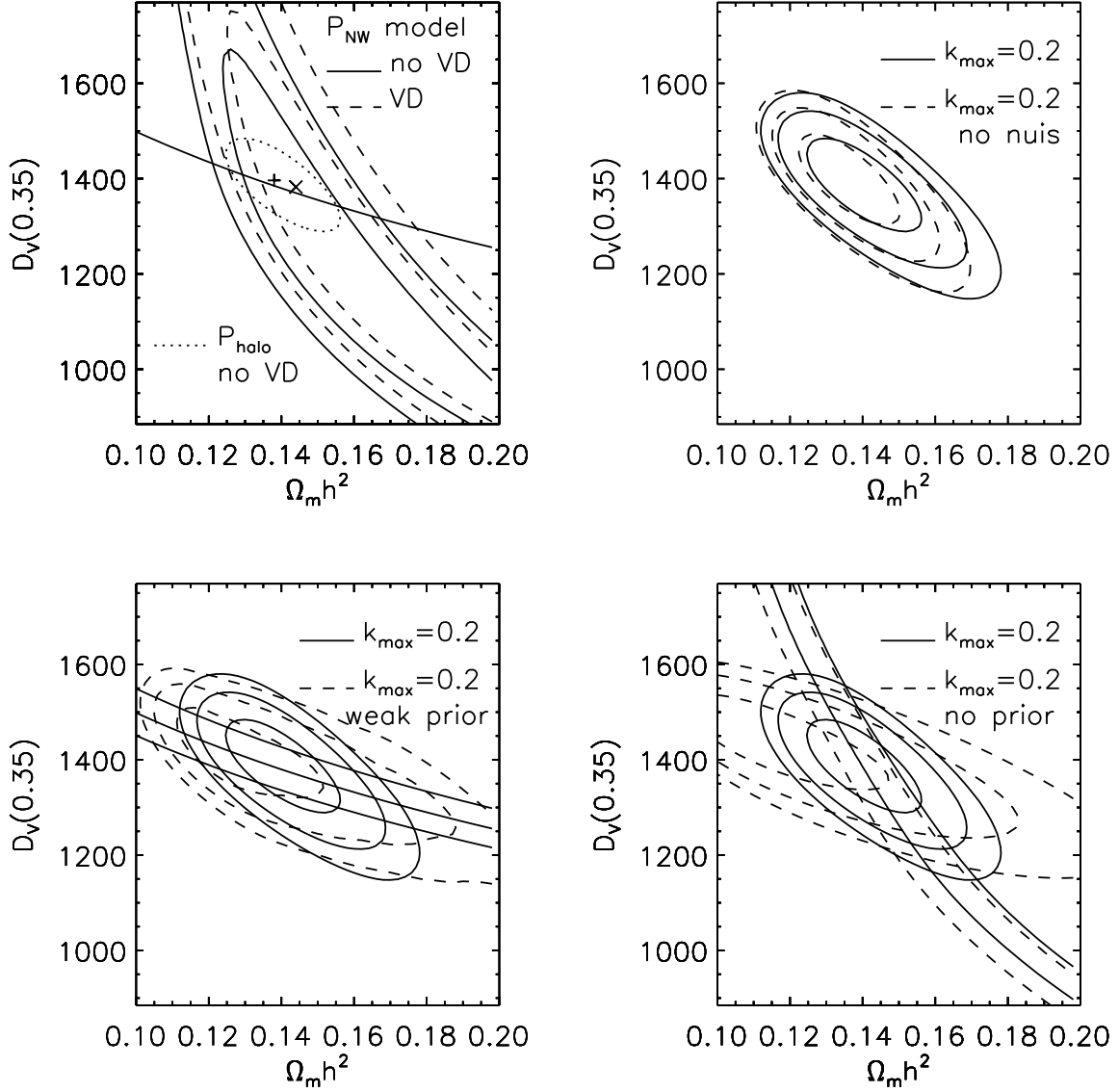


**Figure C1.** Effects of velocity dispersion and nuisance parameters on constraints from the LRG DR7  $\hat{P}_{halo}(k)$  for a  $\Lambda$ CDM model. In each panel we hold  $\Omega_b h^2 = 0.02265$  and  $n_s = 0.960$  fixed. *Upper left panel:*  $\Delta\chi^2 = 2.3$  and  $6.0$  contours for the  $\hat{P}_{halo}(k)$  fit to a no-wiggles model with no central velocity dispersion (solid) and extreme velocity dispersion (dashed). The  $\Delta\chi^2 = 2.3$  for the fiducial model with BAO features is shown for comparison by the dotted line. The cross shows the maximum likelihood point for our fiducial model, while the 'X' shows it for the extreme velocity dispersion model. The solid line indicates  $r_s/D_V(0.35) = 0.1097$ , demonstrating that adopting the velocity dispersion model shifts the likelihood surface along constant  $r_s/D_V(0.35)$ . *Upper right panel:*  $\Delta\chi^2 = 2.3, 6.0,$  and  $9.3$  contours. The solid contours use our fiducial marginalization over  $b_0^2, a_1,$  and  $a_2$  (as in Fig. 5), while in the dotted contours fix  $a_1 = a_2 = 0$  and  $b_0^2$  to the value which minimizes  $\chi^2$ . *Lower left panel:* The solid contours as in Fig. 5, while the dashed contours take the minimum  $\chi^2$  value for which  $|F(k = 0.1 h \text{ Mpc}^{-1})|/b_0^2 < 0.2$  and  $|F(k = 0.2 h \text{ Mpc}^{-1})|/b_0^2 < 0.5$ . *Lower right panel:* The solid contours as in Fig. 5, while the dashed contours minimize  $\chi^2$  with no restrictions on  $a_1$  and  $a_2$ . For comparison with the fiducial nuisance restrictions, the solid lines enclose the region where for the best-fitting  $\chi^2$ ,  $|F(k = 0.1 h \text{ Mpc}^{-1})|/b_0^2 < 0.04$  and the dashed lines enclose  $|F(k = 0.2 h \text{ Mpc}^{-1})|/b_0^2 < 0.1$ .

of Fig. C1. The systematic shift in the contours between the zero and extreme central velocity dispersion model is small compared to the width of the  $\Delta\chi^2 = 2.3$  constraint (dotted curve). When we marginalize over nuisance parameters  $b_0^2, a_1,$  and  $a_2$ ,  $\Delta\chi^2$  between the maximum likelihood model values for the zero and extreme velocity dispersion models is  $\sim 0.3$ . If one instead adopts the  $a_1, a_2,$  and  $b_0^2$  values which minimize  $\chi^2$ , the shift decreases to  $\Delta\chi^2 \sim 0.1$ ; the difference is because the preferred nuisance parameters  $a_1$  and  $a_2$  in the no velocity dispersion model are closer to

the boundary of the allowed values. These  $\Delta\chi^2$  values are approximately the same when considering a fit to the model with or without BAO wiggles. This shift is small compared to the statistical errors, and since the velocity dispersion model considered is extreme compared with the available estimates in the literature (Skibba et al. prep; Coziol et al. 2009), we can safely neglect this systematic uncertainty in the present analysis.

Within our fiducial nuisance parameter bounds and using our fiducial model with no central galaxy velocity dis-

persion, we have verified that the effect of the nuisance parameters in Eqn. 15 is small on the  $\hat{P}_{halo}(k)$  cosmological parameter constraints. The preferred nuisance parameters are off-center in the allowed  $a_1 - a_2$  space, although not at the boundary:  $\langle F_{nuis}(0.1 h \text{ Mpc}^{-1})/b_0^2 \rangle = 0.016$  and  $\langle (F_{nuis}(0.1 h \text{ Mpc}^{-1}) - F_{nuis}(0.2 h \text{ Mpc}^{-1}))/b_0^2 \rangle = 0.060$ , where we have computed a likelihood-weighted average over the DR7-only constraints. The upper right panel of Fig. C1 shows  $\Delta\chi^2 = 2.3, 6.0,$  and  $9.3$  contours where  $a_1 = a_2 = 0$  and  $b_0^2$  is varied to minimize  $\chi^2$  (dashed contours) compared to our fiducial marginalization over  $b_0^2, a_1$  and  $a_2$  (solid contours). Allowing nuisance parameters to account for our imperfect modeling induces both a small shift and widening of the likelihood surface. The difference in the contours is negligible when  $\chi^2$  is evaluated instead at the values  $a_1$  and  $a_2$  that minimize  $\chi^2$ . Therefore the hard boundary we impose in  $a_1 - a_2$  space does not seriously affect the likelihood contours, and  $a_1$  and  $a_2$  are not strongly degenerate with the cosmological parameters constrained by  $\hat{P}_{halo}(k)$  when  $a_1$  and  $a_2$  are tightly constrained by the arguments in Section 4.3.

However, when one substantially relaxes the constraints on the nuisance function, the constraints from the power spectrum shape degrade. The lower right panel of Fig. C1 shows how the  $\chi^2 = 2.3, 6.0,$  and  $9.3$  constraints relax when  $a_1$  and  $a_2$  are chosen to minimize  $\chi^2$  such that  $F_{nuis}(k = 0.1 h \text{ Mpc}^{-1})/b_0^2 < 0.2$  and  $F_{nuis}(k = 0.2 h \text{ Mpc}^{-1})/b_0^2 < 0.5$ . While the constraints on  $r_s/D_V(0.35)$  are unchanged, the shape information is degraded. The effects of scale dependent halo bias are well below these allowed deviations (Smith et al. 2007), and we have argued that our reconstruction of the halo density field should leave much smaller uncertainties as well. The dashed contours in the lower right panel of Fig. C1 show a further broadening of the constraints when  $a_1$  and  $a_2$  are varied without restriction to minimize  $\chi^2$ . For comparison with the adopted nuisance restrictions, the bottom right panel of Fig. C1 also shows the regions where the best-fitting nuisance parameters satisfy  $|F_{nuis}(k = 0.1 h \text{ Mpc}^{-1})|/b_0^2 < 0.04$  (solid lines) and  $|F_{nuis}(k = 0.2 h \text{ Mpc}^{-1})|/b_0^2 < 0.1$  (dashed lines). The width of this region is smaller than the statistical errors derived from the shape constraint, which are shown in the upper left panel. Consequently, it is unsurprising that our marginalized likelihood contours with the fiducial nuisance restrictions deviate only slightly from the contours where  $a_1 = a_2 = 0$ . Finally we note that for the models with and without velocity dispersion, the likelihood-weighted best-fitting nuisance functions have small deviations from one at  $k = 0.1 h \text{ Mpc}^{-1}$  ( $< 2\%$ ), the region containing most of the shape information. The two models differ in the quasi-linear regime:  $\langle (F_{nuis}(0.1 h \text{ Mpc}^{-1}) - F_{nuis}(0.2 h \text{ Mpc}^{-1}))/b_0^2 \rangle = -0.033$  for the velocity dispersion model and  $0.060$  without velocity dispersion. However, we cannot distinguish between velocity dispersion and other modeling uncertainties to explain the shape of the nuisance function preferred by the data. Moreover, using the velocity dispersion model does not improve the overall  $\chi^2$  of the fit.

We conclude that, for this data set, the statistical errors are comfortably larger than the errors from modeling uncertainties.